Check for updates

RESEARCH ARTICLE

REVISED Hidden processing drivers of thermoelectric performance in tetrahedrites

[version 2; peer review: awaiting peer review]

Catarina Quitério[1-3], kalpna Rajput[1], Konstantina Iordanidou[1], Vetle Øversjøen[1], Daniel Marchand[4], Salah Amedi[5], Ana Sá[6], Paulo Luz[6], Alvise Bianchin[7], Marcin Rosiński[8], Daniela Gomes[2], Francisco Molina-Lopez[3], Filipe Neves[6], Patricia Almeida Carvalho[1,9]

[1]Sustainable Energy Technology, SINTEF, Oslo, 0373, Norway
[2]CENIMAT|i3N, Department of Materials Science, School of Science and Technology, NOVA University, Caparica, 2829-516, Portugal
[3]Department of Materials Engineering, KU Leuven, Leuven, 3001, Belgium
[4]Metal Production and Processing, SINTEF, Oslo, 0373, Norway
[5]Process Technology, SINTEF, Oslo, 0373, Norway
[6]Materials for Energy Unit, National Laboratory for Energy and Geology, Lisbon, 1649-038, Portugal
[7]MBN Nanomaterialia srl, Carbonera, 31050, Italy
[8]GeniCore Genicore Sp. z o.o., Warsow, 01-919, Poland
[9]CeFEMA, Departament of Chemical Engineering, Instituto Superior Técnico, University of Lisbon, Lisbon, 1049-001, Portugal

v2 **First published:** 30 Jun 2026, **6**:221
https://doi.org/10.12688/openreseurope.24147.1
Latest published: 20 Oct 2026, **6**:221
https://doi.org/10.12688/openreseurope.24147.2

Abstract

Tetrahedrites are promising thermoelectric materials owing to their intrinsically low thermal conductivity and earth-abundant constituent elements. However, reported performance varies widely across the literature, with unclear compositional trends that hinder the development of reliable optimisation strategies. Here, we combine a large-scale meta-analysis of 276 experimental data series with targeted microstructural characterisation and first-principles calculations to decouple compositional effects from differences in sample quality. After normalising the thermoelectric figure of merit (*zT*) for its temperature dependence, we find that most dopant classes do not produce statistically robust performance improvements over undoped tetrahedrite. Instead, processing-induced variation emerges as the dominant source of performance scatter. Our analysis identifies porosity generated by gas evolution during sintering as a major hidden variable that obscures intrinsic transport behaviour and masks dopant-specific trends. Because heat-carrying phonons in tetrahedrites already exhibit near-atomic-scale mean free paths, microstructural defects provide only marginal further reductions in

Open Peer Review

Approval Status *AWAITING PEER REVIEW*

Any reports and responses or comments on the article can be found at the end of the article.

lattice thermal conductivity, while substantially compromising electrical connectivity. Systematic first-principles calculations further show that Fe is electronically distinct among dopants, introducing localised states near the valence-band edge, consistent with the only statistically significant doping response — a detrimental one — observed in the meta-analysis. These findings demonstrate that thermoelectric performance in tetrahedrites is currently governed more by processing quality and the resulting microstructure than by composition. More broadly, this work redirects optimisation efforts from purely compositional fine-tuning toward rigorous processing control, quantitative microstructural characterisation and standardised transport-property benchmarking, providing a transferable framework for thermoelectric materials development.

Plain Language summary

Tetrahedrites are a family of materials with a useful talent: they can convert waste heat into electricity. These compounds are promising because they naturally impede heat flow and are made from relatively common elements. Yet their potential has been clouded by inconsistency: different studies report widely varying performance, and it has remained unclear whether adjusting their chemical composition truly improves performance. In this study, we analysed 276 sets of published experimental data, examined selected samples, and used computer calculations to separate the effects of chemistry from those of sample quality. Once temperature differences were taken into account, most added elements, or dopants, did not clearly improve performance compared with undoped tetrahedrite. Instead, much of the variation between studies appears to come from how the samples are produced. A key hidden culprit is porosity: tiny holes that can form during sintering, the high-temperature process used to make solid samples. These pores can distort measured properties and obscure the real role of different dopants. This is especially important because tetrahedrites already block heat very effectively at extremely small length scales. Adding more structural disorder therefore brings little extra benefit for reducing heat flow, whilemaking it harder for electricity to move through the material. The calculations show that iron changes the electronic structure differently from other dopants, and the data confirm that it is the only dopant with a statistically clear, harmful, effect. Overall, the study shows that improving tetrahedrites is not simply a matter of changing their chemical composition. Their performance depends more on careful processing and internal structure. Future progress will require careful material production, closer attention to microstructure, and more consistent ways of measuring and comparing performance.

Keywords

Tetrahedrites, Thermoelectric properties, Porosity, Microstructure, Doping, DFT calculations

This article is included in the Horizon Europe gateway.

Corresponding authors: Catarina Quitério (catarina.quiterio@kuleuven.be), Patricia Almeida Carvalho (patricia.carvalho@sintef.no)

Author roles: Quitério C: Data Curation, Formal Analysis, Investigation, Methodology, Software, Validation, Visualization, Writing – Original Draft Preparation, Writing – Review & Editing; **Rajput k**: Data Curation, Formal Analysis, Investigation, Methodology, Validation, Visualization, Writing – Review & Editing; **Iordanidou K**: Formal Analysis, Investigation, Software, Validation, Visualization, Writing – Original Draft Preparation, Writing – Review & Editing; **Øversjøen V**: Data Curation, Investigation, Methodology, Validation, Visualization, Writing – Review & Editing; **Marchand D**: Data Curation, Formal Analysis, Investigation, Software, Validation, Writing – Review & Editing; **Amedi S**: Investigation, Validation, Writing – Review & Editing; **Sá A**: Investigation, Methodology, Validation, Visualization, Writing – Review & Editing; **Luz P**: Investigation, Validation, Writing – Review & Editing; **Bianchin A**: Investigation, Methodology, Resources, Writing – Review & Editing; **Rosiński M**: Investigation, Methodology, Resources, Writing – Review & Editing; **Gomes D**: Resources, Supervision, Writing – Review & Editing; **Molina-Lopez F**: Resources, Supervision, Writing – Review & Editing; **Neves F**: Conceptualization, Funding Acquisition, Investigation, Project Administration, Resources, Supervision, Validation, Writing – Review & Editing; **Almeida Carvalho P**: Conceptualization, Formal Analysis, Funding Acquisition, Investigation, Methodology, Project Administration, Resources, Supervision, Validation, Visualization, Writing – Original Draft Preparation, Writing – Review & Editing

Competing interests: No competing interests were disclosed.

Grant information: This research was funded by the Horizon Europe grant Sustainable Energy Harvesting Systems based on Innovative Mine Waste Recycling (project 101058632 — START).
The funders had no role in study design, data collection and analysis, decision to publish, or preparation of the manuscript.

Copyright: © 2026 Quitério C *et al*. This is an open access article distributed under the terms of the Creative Commons Attribution License, which permits unrestricted use, distribution, and reproduction in any medium, provided the original work is properly cited.

How to cite this article: Quitério C, Rajput k, Iordanidou K *et al.* **Hidden processing drivers of thermoelectric performance in tetrahedrites [version 2; peer review: awaiting peer review]** Open Research Europe 2026, **6**:221 https://doi.org/10.12688/openreseurope.24147.2

First published: 30 Jun 2026, **6**:221 https://doi.org/10.12688/openreseurope.24147.1

REVISED **Amendments from Version 1**

Some minor errors, typos and grammatical improvements.

Any further responses from the reviewers can be found at the end of the article

Introduction

More than 60% of global primary energy consumption is ultimately dissipated as waste heat[1], and recovering this energy could significantly contribute to reducing greenhouse gas emissions. Thermoelectric (TE) devices provide a direct route to waste-heat harvesting by converting temperature gradients into electricity.[2,3] Their solid-state nature enables silent, reliable operation and long service lifetimes with minimal maintenance owing to the absence of moving parts.[4,5] TE generators can be integrated across a wide range of energy systems,[6] with demonstrated applications ranging from gas pipelines, spacecraft power systems, and marine engines to domestic biomass stoves and wearable electronics.[7–13]

Unlike mechanical heat engines, which are typically suited to large-scale power generation,[14,15] thermoelectrics offer distinct advantages in waste-heat recovery applications where simplicity, reliability, and design flexibility often outweigh the need for maximum efficiency. In addition, they are also well suited to low-power operation[16] and cooling applications.[17] Nevertheless, the widespread deployment of TE technologies remains constrained by the scarcity, toxicity, and cost of many high-performance materials.[18–20] Consequently, there is a strong need for compounds that combine competitive TE performance with earth-abundant composition.

In this context, tetrahedrite ($Cu_{12}Sb_4S_{13}$) emerges as a compelling candidate for mid-temperature TE power generation ($\sim$ 350 °C).[21,22] Tetrahedrite is a non-toxic, low-cost p-type semiconductor and the most abundant sulphosalt in the Earth's crust. As it is often discarded as gangue during Cu and Zn mining, it offers an opportunity for waste valorisation and resource efficiency,[23–25] reducing reliance on primary materials while mitigating environmental impacts associated with sulphide waste, including acid mine drainage.[26]

High TE efficiency requires a large Seebeck coefficient (S), high electrical conductivity (σ), and low thermal conductivity (κ), the latter comprising an electronic component from charge-carrier transport (K_e) and a lattice component from phonon transport (K_l).[2,13] However, these properties cannot be optimised independently because κ_e is coupled to σ through the Wiedemann–Franz law. These competing requirements are captured by the dimensionless figure of merit,

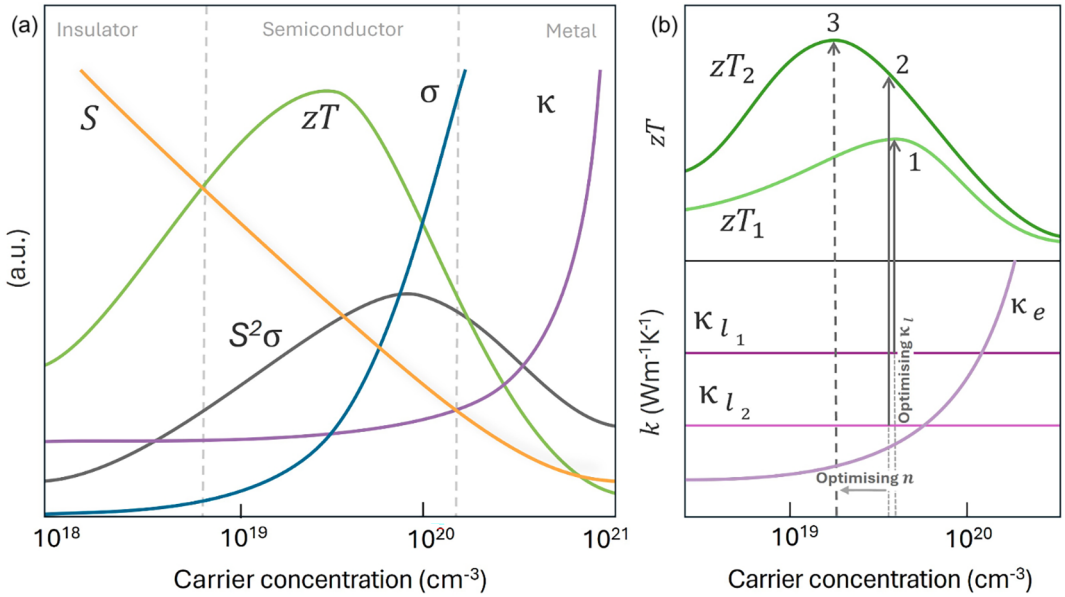

Figure 1. Tuning TE performance. (a) Transport properties vs. carrier concentration across material classes. (b) Strategies to maximise zT: reducing the relatively n-independent κ_l through enhanced phonon scattering (1→2), and lowering n to decrease κ_e while increasing S, shifting performance toward the optimal regime (3). Adapted from Snyder *et al.*[32]

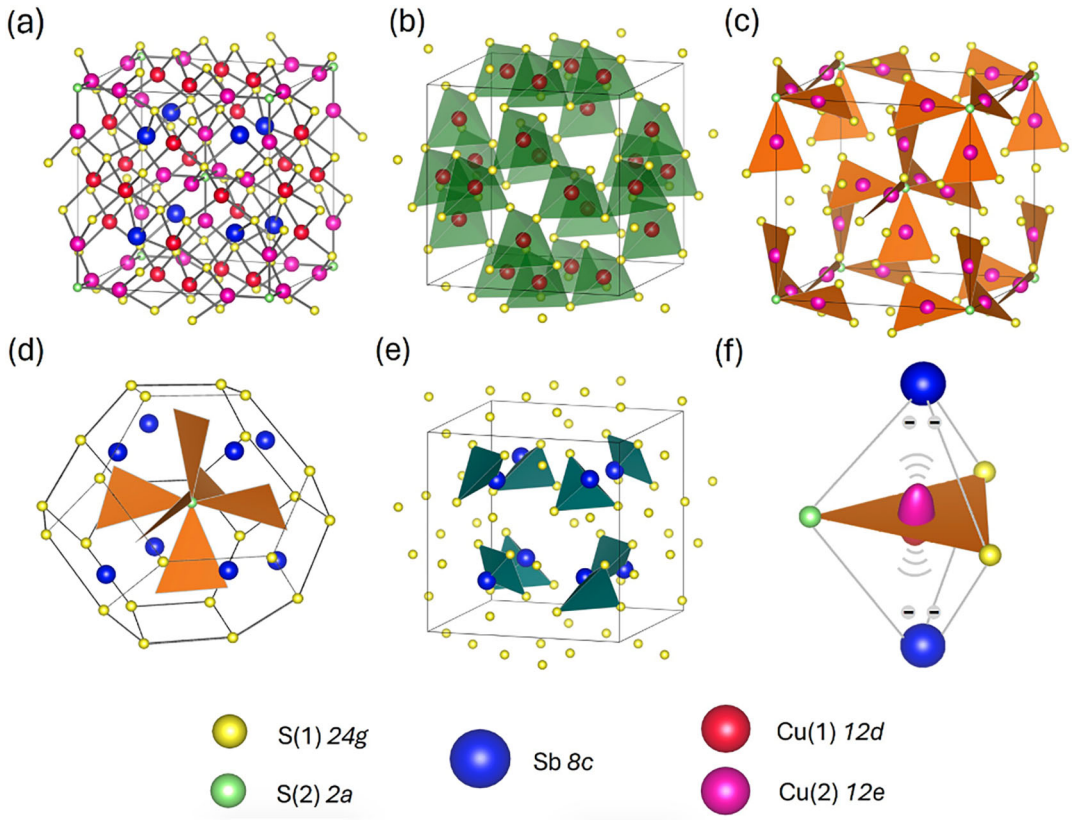

Figure 2. Tetrahedrite crystal structure. (a) Conventional unit cell of Cu12Sb4S13. (b) CuS_4 tetrahedra each formed with one Cu(1) (12*d*) and four S(1) (24*g*) atoms. (c) Cu(2) (12*e*) trigonal-planar coordinated with two S(1) (24*g*) and one S (2) (2*a*) atoms. (d) Cu_6S_{13} cluster inside an S(1) truncated octahedron. (e) SbS_3 trigonal pyramids where Sb is coordinated by S(1). (f) Cage-like Sb[CuS_3]Sb trigonal-bipyramid framework enclosing each Cu(2), which rattles between Sb lone pairs. The displacement ellipsoid is shown at the 90% probability level. Structural models created with VESTA.[42]

defined as $zT = S^2\sigma T/(\kappa_e + \kappa_l)$.[27–29] Efficient TE materials are typically semiconductors, in which the characteristic dependence of σ, S, and κ on carrier-concentration (n) maximizes zT[30] (Figure 1a). Performance can be further enhanced by suppressing κ_l through phonon scattering,[31] in combination with tuning n to lower K_e and increase S. Provided the associated decrease in σ remains moderate, this shifts transport toward the optimal balance of transport properties[32] (Figure 1b).

Interest in tetrahedrite as a TE material grew in the 2010s when its exceptionally low K_l was reported.[23,33] The compound crystallises in a complex body-centred cubic structure (space group $I\bar{4}3m$) with a lattice parameter $a \approx 10.33$ Å and 58 atoms per conventional unit cell[34] (Figure 2a). The framework contains two distinct Cu sites (Cu(1) at 12*d* and Cu(2) at 12*e*) and two distinct S sites (S(1) at 24*g* and S(2) at 2*a*), while Sb occupies a single position (8*c*).[35,36] Cu(1) is tetrahedrally coordinated by S(1) (Figure 2b), whereas Cu(2) adopts a trigonal–planar coordination with two S(1) and one S(2) atoms, forming CuS_3 units on {110} planes (Figure 2c). Six such triangles assemble into Cu_6S_{13} clusters centred on S (2), generating sodalite-like truncated octahedra[37] (Figure 2d). Sb is coordinated by three S(1) nearest-neighbours in pyramidal SbS_3 units (Figure 2e). In addition, it interacts with nearby CuS_3 units resulting in trigonal-bipyramidal Sb[CuS_3]Sb cages with an enclosed central Cu(2) atom, reminiscent of frameworks found in skutterudites and clathrates[38] (Figure 2f). The stereochemically active lone electron pairs on Sb atoms generate electrostatic repulsion of the encapsulated Cu(2) atoms, driving a characteristic rattling motion perpendicular to the trigonal S plane.[39,40] Displacements approaching 0.8 Å induce pronounced lattice anharmonicity, strongly enhancing thermal phonon scattering and underpinning the intrinsically low K_l.[41]

The oxidation state of Cu in tetrahedrite remains debated. The most common interpretation describes tetrahedrite as a mixed-valence system, in which tetrahedrally coordinated Cu(1) ions adopt both Cu^+ and Cu^{2+} states, often represented as: $\left(Cu_4^{+}Cu_2^{2+}\right)^{t}\left(Cu_6^{+}\right)^{tr}\left(Sb_4^{3+}\right)^{\pi}\left(S_{12}^{2-}\right)^{t}\left(S_1^{2-}\right)^{o}$, where t, tr, π, and o denote triangular, tetrahedral, pyramidal, and

octahedral coordination, respectively.[43] The two Cu^{2+} ions, located in the tetrahedral Cu(1) sites, introduce holes into the structure[40,43,44] and are preferentially substituted during doping, which is consistent with the commonly reported limit of two substitutional atoms per formula unit.[45] This model is supported by spectroscopic studies, including near-edge X-ray absorption fine structure (NEXAFS) and X-ray photoelectron spectroscopy (XPS), which report signatures of both Cu^{+} and Cu^{2+} states.[46–48] However, the Cu^{2+} features are typically weak and often approach the noise level, limiting the robustness of the assignment. Moreover, strong electronic delocalisation within metal–sulphur bonds, characteristic of Cu-rich sulphides, further challenges the validity of a Cu mixed-valence description.

An alternative interpretation proposes that all Cu ions remain monovalent, with unoccupied states arising from band-structure effects.[24,49] Consistent with this model, density functional theory (DFT) calculations indicate that two holes per formula unit—corresponding to the formal $Cu^{+}_{12}Sb^{3+}_{4}S^{2-}_{12}$ composition—are delocalized throughout the lattice (Figure 2d).[37] Tetrahedrite is predicted to be an indirect band-gap semiconductor with a gap of 1.2–1.7 eV and a Fermi level located near, or even within, the valence band, giving rise to highly degenerate p-type behaviour.[23,50] In this model, strong Cu $3d$ – S $3p$ hybridisation dominates the valence band, promoting hole delocalisation and enabling quasi-metallic transport.

The electronic flexibility of tetrahedrites gives rise to an accommodating crystal that supports multiple chemical substitutions as evidenced by the partial substitution of Cu with Fe, Zn and Ag, and of Sb with As in natural tetrahedrites.[25,51,52] This versatility has enabled a broad range of doping strategies in synthetic materials.[22,53] However, despite extensive exploration, reported TE performance of tetrahedrites varies inconsistently across the literature reflecting differences in doping strategy, synthesis route and sintering conditions.

Existing data resources provide only limited support for systematic studies: for example, the Starrydata database compiles transport properties from the literature but currently includes only a small number of tetrahedrite entries (≈20), restricting its utility for comparative studies.[54] Similarly, available reviews lack a unified framework capable of separating the respective contributions of composition and processing.[55–57]

To address this gap, a comprehensive meta-analysis was performed using virtually all available transport data for mechanochemically synthesised, pressure-assisted sintered tetrahedrites, spanning 58 studies and more than 6,000 data points. Performance was normalised to account for the intrinsic temperature dependence of zT, enabling statistically consistent comparison across compositions and processing conditions. Complementary experimental observations and first-principles calculations were used to interpret and contextualise the results.

The analysis reveals that, at the current stage of development, dopant chemistry plays a secondary role in determining TE performance, whereas processing quality dominates the observed variability. Beyond tetrahedrites, this work illustrates how literature-scale datasets can reveal hidden processing variables in functional materials, for which nominal composition is often overemphasised, and provides a transferable framework for separating intrinsic chemical contributions from extrinsic microstructural variability across TE materials.

Methods

Data analysis

Data were extracted from published figures through a combination of automated and manual digitisation. Automated retrieval was performed using PlotExtract, an artificial intelligence-based graph-digitisation workflow,[58] followed by systematic validation against the original figures. In cases where overlapping curves, dense data points, or graphical annotations prevented reliable automated parsing, manual digitisation was performed using WebPlotDigitizer.[59] Approximately 1,000 curves were processed, yielding more than 6,000 transport-property data points representing 276 tetrahedrite samples. The compositions and corresponding references are listed in Table 1. Approximately half of the dataset required manual digitisation owing to limitations in fully automated extraction. The resulting database is openly available.[60] Nanoparticle-based materials,[61–66] composites,[67–69] mineral-derived samples,[70,71] and materials prepared by alternative routes (e.g., solvothermal synthesis)[72–75] were excluded to ensure methodological comparability, although these classes may be incorporated in future updates.

For cross-study comparability, all TE properties were evaluated at 350 °C (interpolated where necessary), as this temperature lies safely below reported decomposition onsets (492°C for natural tetrahedrite[76] and 400°C for $Cu_{10}Cd_2Sb_4S_{13}$).[77] Quantile regression was employed to estimate conditional zT quantiles as functions of measurement temperature and composition using, respectively, first- and second-order polynomial models fitted with the standard quantile loss function. This approach is well suited to aggregated literature datasets, in which variability in composition, synthesis routes, and measurement conditions produces heteroscedastic distributions. In this context, quantile regression

provides a robust statistical framework, as it estimates conditional percentiles of the response variable without assuming normally distributed or homoscedastic residuals.

Statistical analyses were performed to compare the undoped reference subset with each dopant subset. The subsets were constructed by excluding co-doped samples, while pooling measurements across all doping levels for a given dopant to increase statistical power. Due to skewed distributions and unequal group sizes, differences were assessed using two-sided Mann–Whitney U tests at a significance level of $\alpha = 0.05$. Effect sizes were estimated using the rank-biserial correlation coefficient, defined as $r_{rb} = 1 - 2U/(N_{undoped}.N_{doped})$, where N denotes the sample size. The undoped group was treated as the reference, such that the sign of r_{rb} reflects the direction of the difference. Effect sizes were categorised as none ($|r_{rb}| < 0.1$), small ($0.1 \leq |r_{rb}| < 0.3$), medium ($0.3 \leq |r_{rb}| < 0.5$), or large ($|r_{rb}| \geq 0.5$).

Experimental

Experimental investigations were performed to support and contextualise the findings of the data analysis. Undoped and Fe,Zn-doped ($Cu_{11}Fe_{0.5}Zn_{0.5}Sb_4S_{13}$) samples were produced by mechanochemical synthesis and spark plasma sintering (SPS). Elemental powders were mechanically alloyed in a Retsch EMAX high-energy ball mill at 1200 rpm for 2 h using 125 mL stainless steel jars and 12 mm stainless steel balls, with a ball-to-powder ratio of 10:1, under an argon atmosphere to prevent oxidation. Consolidation was performed in a Genicore U-FAST system, under vacuum, using graphite dies, at temperatures in the range of 340–500°C and under uniaxial pressures of 60–70 MPa. The resulting bulk densities were measured using the Archimedes method.

Crystal structure and phase purity were confirmed by X-ray diffraction (XRD) using a PANalytical Empyrean diffractometer in Bragg-Brentano geometry with Cu Kα radiation, a step size of 0.013° in 2θ, and an acquisition time of 148.92 s per step.

Microstructures were examined by field-emission scanning electron microscopy (SEM) using an FEI NanoLab 600 instrument in backscattered electron (BSE) mode at 8 kV, following standard metallographic sample preparation. Image analysis was carried out with ImajeJ. The TE properties of the sintered samples were measured using a LINSEIS LZT-Meter (LZT L33) under a helium atmosphere at 1 bar.

Density functional theory calculations

To further complement the data analysis, a systematic spin-polarised DFT study was conducted to elucidate the effects of representative dopants on the electronic structure of $Cu_{12-x}M_xSb_4S_{13}$, with M = Mn, Fe, Co, Ni and Zn. First-principles calculations were performed using the Vienna ab initio Simulation Package (VASP),[78,79] with electron–ion interactions described by the projector-augmented-wave (PAW) method,[80] and exchange–correlation treated within the Perdew-Burke-Ernzerhof (PBE) generalised gradient approximation.[81] A plane-wave kinetic energy cut-off of 500 eV was employed. The Brillouin zone was sampled using a $10\times10\times10$ k-point mesh for structural relaxations and a $20\times20\times20$ mesh for density-of-states calculations. Doped compositions were modelled using 29-atom unit cells (one formula unit), with a representative substitution level of $x = 1$. Atomic positions and cell volume were relaxed while constraining the cell shape.

Band-decomposed charge densities were analysed to examine the spatial distribution of valence-band states near the Fermi level, and Bader charge analysis was performed to evaluate site-resolved charge trends. Additional calculations using the SCAN meta-GGA functional[82] were conducted to verify the robustness of the observed charge-distribution trends.

Results and discussion

Temperature dependence of thermoelectric performance

Benchmarking TE materials requires accounting for the temperature dependence of zT. The hexagonal binning heatmap in Figure 3a presents the distribution of experimental zT values for tetrahedrites as a function of measurement temperature, with overlaid linear quantiles at the 50%, 75% and 95% levels. The corresponding scatter plot (together with hexagonal binning plots for S, σ and κ) is provided in Figure S1 in the Supplementary Materials.[83] The dispersion in zT values is substantial but comparable to that reported for other TE materials, such as skutterudites and half-Heusler alloys, for which meta-analyses have also been conducted.[84,85] As shown in Figure 3b, a similarly wide dispersion is observed among undoped samples (the largest nominally identical subset, with the corresponding scatter plot also provided in Figure S1[83]). This demonstrates that, beyond dopant-induced modifications to the electronic structure, the dispersion in Figure 3a arises from variations in processing conditions and measurement methodologies across independent studies.

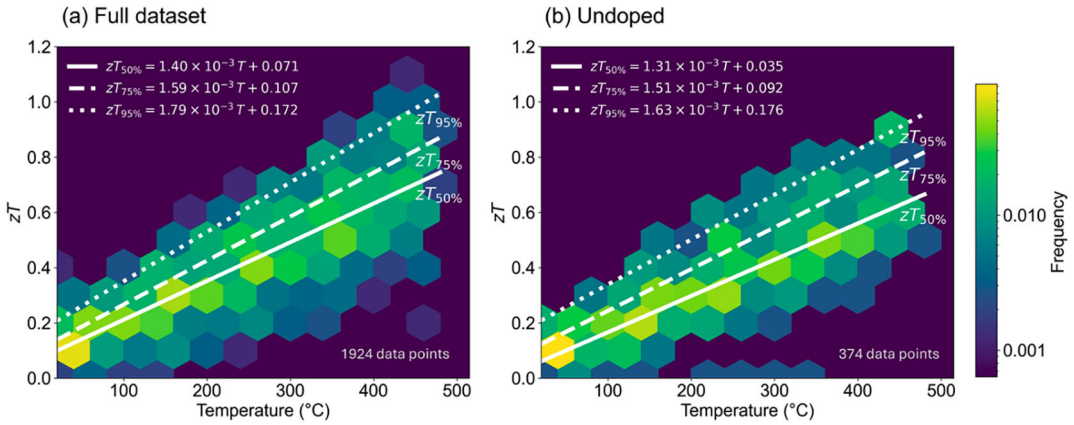

Figure 3. Hexagonal binning plots of *zT vs.* measurement temperature. a) full dataset and (b) undoped tetrahedrites. Linear quantile regressions corresponding to 50%, 75%, and 95% levels are overlaid. The colour scale represents frequency (number of data points within each hexagon normalized by the total number of points in the dataset).

Near-zero zT outliers (see Figure S1a and b[83]) are likely to substantially underestimate the intrinsic TE performance of the tested compositions, systematically skewing the temperature-dependent zT distributions toward underperforming samples as evidenced by the pronounced lower-tails of the heatmaps in Figure 3a and b. Therefore, standard central-tendency metrics, such as the mean or median, fail to reliably capture the performance of well-processed materials. The linear quantile regressions address this limitation by emphasising the upper portion of the distributions where samples produced under optimised processing conditions are expected to reside. Within this framework, the 75% quantile emerges as a pragmatic benchmark for assessing high-quality tetrahedrites, yielding $zT_{75\%}(350°C) \approx 0.7$ for the full dataset and ≈ 0.6 for undoped tetrahedrite.

At the upper end of the temperature-dependent zT distributions, the reported values are seldom reproduced and carry substantial propagated errors. Typical relative uncertainties exceed 7% for σ, 5% for S, and 10% for K.[86] The latter is calculated from $K = D\ C_p\ \lambda$, where D is density, C_p is specific heat capacity, and λ is thermal diffusivity, which alone contributes an uncertainty of ~7%.[86] As a result, the compounded uncertainty in zT can exceed 15%, complicating quantitative cross-study comparisons.[87,88] In this context, the 95% quantile is used to represent optimised performance, as it mitigates the influence of high-end outliers. At 350°C, the 95% performance frontier is $zT_{95\%}(350°C) \approx 0.8$ for the full dataset and $\approx$ 0.7 for undoped tetrahedrite. This provides a robust and consistent benchmark for evaluating high-performing samples.

Processing effects

Processing conditions affect the final chemistry and determine the microstructure, thereby shaping TE behaviour. Mechanochemical synthesis is the dominant method for producing tetrahedrites directly from elemental precursors.[89] Milling parameters control the resulting chemical homogeneity, crystallite size, and particle size, as well as the extent of contamination by the milling media and milling atmosphere. Iron contamination from steel milling media is well documented in high-energy ball milling, typically reaching ~1–2 wt.% Fe under conventional conditions and increasing with milling time.[90,91] In addition, contamination by inert gas and by oxygen introduced via leaks or incorporation of passivation layers from milling media surfaces must also be considered.[92] XRD is typically used to confirm phase purity; however, other key properties relevant to consolidation and transport, including particle-size distribution and impurity uptake, are seldom reported, limiting reproducibility and cross-study comparability.

Tetrahedrite powders are typically consolidated by hot pressing (HP) or SPS, two uniaxial pressure–assisted methods that achieve high densification while limiting grain growth.[93] In HP, the die–powder assembly is heated by conventional resistance heating,[94] whereas in SPS, pulsed direct current is passed through the graphite tooling and the compact, enabling substantially higher heating rates and faster consolidation.[95] Alternative approaches such as cold pressing followed by pressure-less sintering and open-die pressing have also been explored.[33,96,97] Die materials such as graphite constitute an additional (yet typically unquantified) source of contamination. Figure 4a compares the different consolidation techniques in terms of zT values measured at 350 °C. Although HP is the most adopted method, both the average zT and its dispersion are comparable across consolidation routes, indicating that the technique chosen is not a determining factor within the explored processing space.

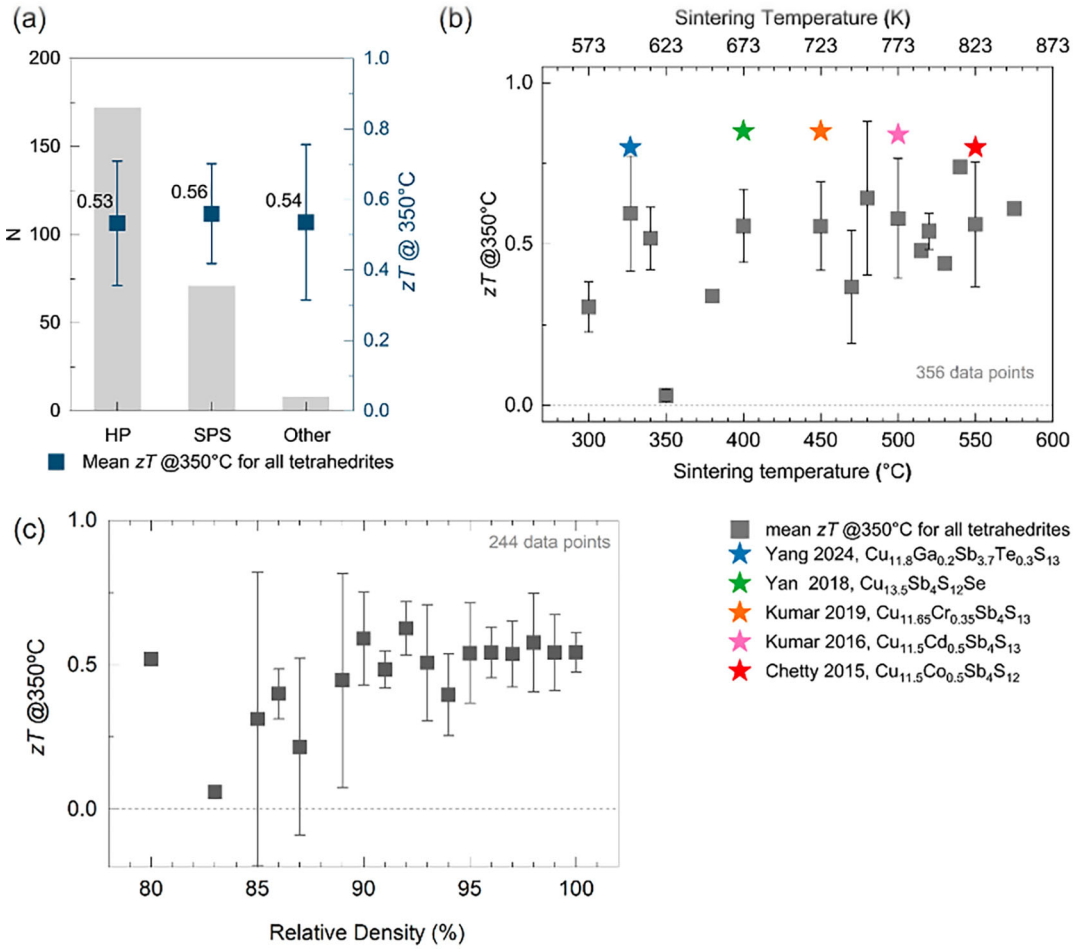

Figure 4. Effect of processing variables. (a) Comparison of consolidation routes in terms of *zT* at 350 °C, where bars represent the number of samples (*N*) processed by each technique in the full datase. (b) *zT* at 350 °C *vs.* sintering temperature for all compositions with notable values (stars) identified in the legend. (c) *zT* at 350 °C *vs.* relative density for all tetrahedrites. Relative density values within ±2% are binned together to reduce visual clutter.

During sintering, a complex interplay of variables governs the final crystallinity and microstructure, ultimately influencing TE performance.[98] Although the sintering temperature is typically a critical processing parameter in materials science, the full dataset shows comparable average performance at 350 °C for samples sintered in the 300–550 °C range, with peak *zT* values (stars) in each temperature class consistently close to 0.8 (Figure 4b). Despite their limited size, similar behaviour is observed for subsets with the same nominal composition, as illustrated for undoped tetrahedrite in Figure S3.[83] This apparent insensitivity to the sintering temperature points to competing temperature-dependent processes that can only be clarified through detailed microstructural characterisation.

Figure 4c presents the average *zT* at 350 °C as a function of relative density for the full dataset. Although relative densities are often referenced to unverified theoretical values, introducing additional variability, a clear dependence of *zT* on relative density is nonetheless evident. Lower-density samples exhibit reduced average *zT* and greater dispersion, whereas for relative densities above 95%, the average *zT* consistently exceeds 0.5 and the spread narrows markedly, indicating improved reproducibility (Figure 4c).

Consistent with recommendations for reliable benchmarking,[99] restricting the analysis to samples with relative densities ≥ 95% (77% of the dataset) substantially reduces scatter (compare Figure S4a[83] with Figure S1a).[83] Nevertheless, the quantile regression envelopes remain essentially unchanged, indicating that both the highest and lowest reported *zT* values are predominantly associated with densities below 95%. Notably, the high-density subset also shows *zT* insensitivity to the sintering temperature (compare Figure S4b[83] with Figure 4b). Data from Heo *et al.*[100] were excluded from Figure 4 because the reported TE properties extend only up to 300 °C (green and yellow stars in Figure S1a),[83]

precluding direct comparison at 350°C. These samples exhibit particularly low relative densities (≤ 88%), leading to markedly reduced K values (~0.2 $Wm^{-1}K^{-1}$) and correspondingly outlying zT behaviour (see Figure S1a).[83]

Microstructural evidence linking processing conditions to TE performance remains scarce for tetrahedrites.[101] To address this gap, undoped, Fe-, Zn- and Fe,Zn-doped tetrahedrites have been produced by mechanochemical synthesis followed by SPS at temperatures in the 340–500°C range. The compositions and processing conditions were selected to probe representative microstructures rather than to perform an exhaustive parametric survey. Powder XRD confirmed tetrahedrite as the dominant phase (Figure S5).[83] All undoped and doped samples sintered across the 340–500 °C range exhibited submicrometre-scale intergranular pores with predominantly rounded morphologies, consistent with internal vapour-pressure build-up driven by sulphur sublimation. Pure sulphur reaches a vapour pressure of 1 atm at 445 °C, underscoring the strong thermodynamic driving force for volatilisation in sulphur-containing compounds and indicating that pore size and distribution are expected to depend strongly on the sintering temperature.

The observations revealed that pore morphology evolves with sintering temperature: larger and less spherical pores at lower temperatures suggest concurrent densification and gas release (Figure 5a), whereas smaller and more spherical pores distributed along the boundaries of polygonal grains reflect capillarity-driven pore equilibration at higher temperatures (Figure 5b). The latter type of pore distribution severely disrupts connectivity between the grains, affecting transport pathways. These results demonstrate competing effects of densification and sublimation-driven pore formation across the sintering temperature range, providing a mechanistic explanation for the apparent insensitivity of zT to the sintering temperature.

Several studies report microstructures of tetrahedrites, yet porosity is typically overlooked.[47,101–119] In most cases, standard metallographic preparation is not employed, or the spatial resolution of the micrographs is inappropriate—either too low to resolve pores or atomically resolved but over a limited field of view—hindering reliable assessment of porosity. Nonetheless, pores similar to those shown in Figure 5 are clearly visible in other SPS-consolidated tetrahedrites[103,109] or can be inferred from published micrographs.[110,113,116–118,120] This suggests that sulphur-driven pore formation is widespread, although rarely explicitly addressed. The phenomenon may be specific to SPS; however, the comparable average zT and standard deviation observed for samples produced by HP (see Figure 4a) indicate that it is likely a general feature. Although pore formation remains to be quantitatively characterised, pervasive porosity contributes to the broad zT variability in the literature (Figure 1).

The influence of porosity on zT is inherently non-trivial because density is not an independent variable but rather a proxy for microstructure. When density variations arise from pores, interpreting K through $K = D\ C_p\ \lambda$ becomes problematic, because this identity, while locally valid, does not rigorously describe effective transport in heterogeneous media. In such systems, macroscopic heat transport is governed by interfacial resistance, tortuosity, and connectivity, resulting in a non-linear relation between D and K.[121,122] Only under restrictive conditions—namely, low porosity, clear scale separation, local thermal equilibrium, and diffusive transport—can an *effective (eff)* description of thermal transport be provided by a

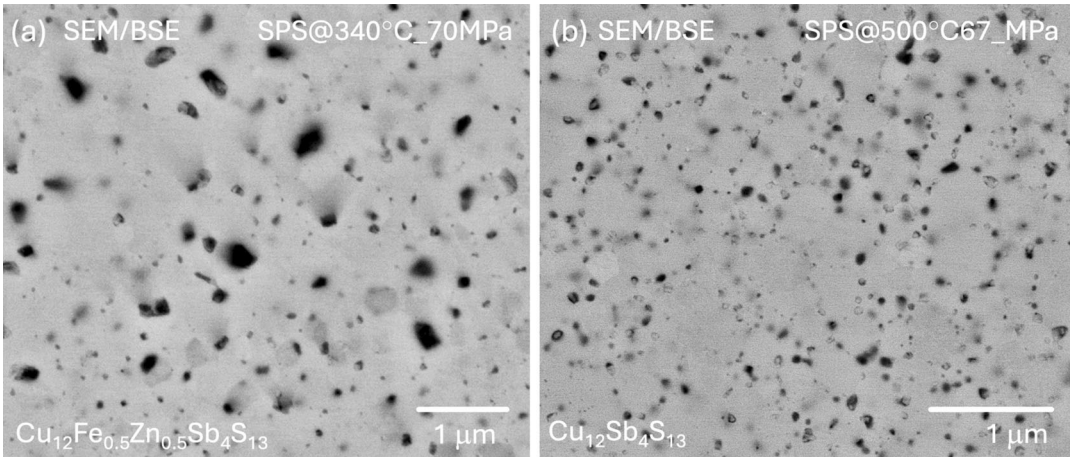

Figure 5. Microstructures of tetrahedrites sintered by SPS. (a) Cu11Fe0.5Zn0.5Sb4S13 at 340°C under 70 MPa (D = 4.9 g.cm−3, 6% porosity and 90 ±70 nm pores), and (b) Cu12Sb4S13 at 500°C under 67 MPa (D = 4.8 gcm−3, 11% porosity and 70 ±40 nm pores). Direct use of D in $\kappa = D.C_p.\lambda$ yields in apparent zT(350°C) = 0.91 and 0.77, respectively (with high level of uncertainty due to the porosity).

proportional $K_{eff} \approx (DC_p)_{eff} \lambda_{eff}$ relation, an approximation possible because both D and C_p are volumetric quantities that can be homogenised through geometric averaging.[121,122] Outside those conditions, however, the use of bulk density to infer K_{eff} leads to inconsistent estimates of zT. The same limitation applies to electrical transport: although $\sigma = n\,e\,\mu$, where e is the elementary charge and μ is carrier mobility, is locally valid, porosity introduces voids and interfaces that reduce μ through energy barriers and disrupt percolation pathways, leading to a non-linear dependence of σ_{eff} on microstructure.[32] Consequently, porosity rarely modifies zT in a predictable manner.

The competition between electronic and thermal transport disruption by microstructural features is particularly relevant in tetrahedrites, where strong intrinsic anharmonicity already confines the mean free paths of heat-carrying phonons to near-atomic length scales.[24,75,123] Green–Kubo and diffuson analyses show that K_l saturates below ~1 nm.[41,123,124] Because pores are orders of magnitude larger than the relevant phonon length scales, they contribute negligibly to additional scattering, with reductions in K_{eff} arising primarily from geometric effects such as reduced solid fraction and increased tortuosity.[125] In contrast, electrical transport remains highly sensitive to connectivity, such that σ typically decreases more strongly than K, rendering net improvements in zT through enhanced porosity unlikely for tetrahedrites.

An apparent exception was reported by Hu *et al.,*[114] who observed that porosity induced in tetrahedrite via sublimation of co-processed BiI_3 produced large reductions in K and high zT values, attributed to reduced heat-conduction pathways and unexpectedly enhanced μ. However, such behaviour is not representative, and incomplete densification can generally be expected to amplify variability in reported transport properties, thereby obscuring intrinsic and dopant-specific trends.

In summary, porosity is not a simple tuning parameter but a coupled perturbation of transport pathways and must be treated explicitly using microstructure-aware frameworks, including effective-medium, percolation, or Boltzmann transport models.[32] Accordingly, controlling sulphur volatilisation and minimising residual porosity is essential for isolating intrinsic TE behaviour and enabling meaningful chemical optimisation of tetrahedrites.

Copper substitution and excess

Substitution of Cu(1) with 3d transition metals is the primary strategy for tuning the TE performance of tetrahedrites. Neutron-diffraction studies show that such dopants, namely Ni and Fe, preferentially occupy the tetrahedrally coordinated 12*d* sites rather than the trigonal 12*e* sites.[102,126] This site selectivity enables control of n while preserving the rattling behaviour of Cu(2) atoms, thereby allowing partial decoupling of electrical and thermal transport. However, substitution of monovalent Cu with higher-valence metals is constrained by charge balance, typically limiting dopant solubility to $x \leq 2$ in $Cu_{12-x}M_xSb_4S_{13}$.

Each $Cu^+ \rightarrow M^{2+}$ substitution reduces hole concentration, shifting the Fermi level toward the band gap, and simultaneously introduces mass and strain disorder that suppresses K_l.[24,50,108] At moderate substitution levels, the reduction in n is offset by an enhancement in S, leading to enhanced zT. Beyond this optimum, further substitution causes excessive carrier depletion, degrading TE performance (see Figure 1b).

A wide range of dopants has been explored owing to the structural flexibility of tetrahedrites (see Table 1 for compositions and references). While most studies focus on 3*d* metals, other elements such as Zn, Ge, Cd and Pb and have also been investigated. In addition, co-doping strategies include substitution of Cu with simultaneously Ni and Zn, or Fe and Zn, as well as substitution at multiple sublattices, namely Cu/Sb (Zn/Bi, Co/Te and Ga/Te), Cu/S (Gd/Se), and Sb/S (Te/Se).

The dependence of zT (350 °C) on Cu content is shown in Figure 6, for compositions with the general formula $(Cu_wM_xT_y)(Sb_{4-i}Q_i)(S_{13-j}R_j)$, where M and T denote elements substituting Cu, and Q and R denote elements substituting Sb and S, respectively. Within the Cu-substitution regime ($w < 12$), second-order polynomial regressions were used to estimate conditional quantiles as a function of Cu content, reflecting the expectation that optimal performance occurs at moderate substitution levels. Typically, heavy Cu substitution ($w < 10.5$) suppresses zT, whereas moderate substitution (w ≈ 11-11.5) enhances performance relative to both undoped materials and samples substituted only at Sb/S sites (all nominally at $w = 12$). Reports on the Cu-excess regime ($w > 12$) remain more limited[127–129] but suggest an increase in zT with increasing Cu content compared to the mean value for $w = 12$ (black square). This behaviour has been attributed to the emergence of a "liquid-like" Cu sublattice with enhanced ionic mobility, which suppresses K_l via reduced phonon mean free paths, consistent with phonon–liquid electron–crystal (PLEC) behaviour.[73,127] This interpretation remains largely phenomenological, as direct evidence for liquid-like Cu dynamics under operating conditions is scarce. Some of the highest-performing compositions occur in this regime, including $Cu_{13.5}Sb_4Se_{13}$,[129] which exhibited zT = 1.1 at 450 °C, corresponding to ≈ 0.85 at 350 °C (star in Figure 6).

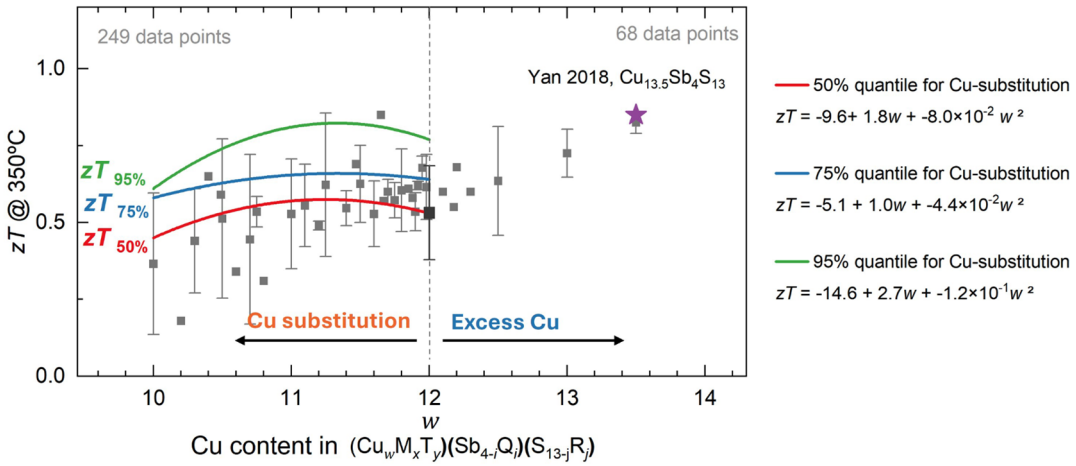

Figure 6. *zT* at 350 °C *vs.* Cu content for $(Cu_wM_xT_y)(Sb_{4-i}Q_i)(S_{13-j}R_j)$, where M and T denote Cu substitution, and Q and R denote Sb and S substitutions, respectively, while *w* = 12-*x*-*y*+*z* with *z* being excess Cu. Compositions with $w < 12$ and $w > 12$ correspond to Cu-substituted and Cu-excess regimes, respectively. Samples with $w = 12$ (58 data points) include undoped and Sb/S-substituted materials. Squares and error bars indicate means and standard deviations. Second-order quantile regressions are shown for $w < 12$. The star denotes a high-performing composition.

Figure 7 presents the average zT and standard deviation at 350 °C for single-dopant Cu substitutions, alongside values for the undoped, Cu excess, and Cu deficiency conditions. Data within each class were pooled across doping levels owing to limited sample sizes. Blue stars denote the highest reported/interpolated zT values at 350 °C, with the corresponding compositions listed in Table S1.[83] zT values obtained at higher temperatures or drawn from studies restricted to temperatures below 350 °C are excluded from Figure 7.

Statistical analysis using the Mann–Whitney U test indicates that, for most dopant classes shown in Figure 7, the differences in zT at 350 °C relative to undoped tetrahedrite are not statistically significant (see Table S2).[83] The exception is Fe doping, which produces a significant reduction in TE performance ($p = 0.022$), a finding particularly relevant given the likelihood of unintentional Fe incorporation during synthesis when using steel milling media.[90,91] The lack of statistical significance reflects limited sample sizes implying that the analysis is underpowered to resolve moderate dopant effects. In addition, since performance depends on dopant concentration (see Figure 6 for $w < 12$), pooling across the substitution levels increases within-class variability. Furthermore, although statistical significance is not observed, several conditions—including Cu excess and deficiency as well and Cr-, Co- and Ni-doping—exhibit medium-to-large effect sizes (r_{rb}), suggesting systematic deviations from the undoped reference (see Table S2).[83]

Collectively, these findings indicate that dopant concentration dependence and extrinsic factors such as measurement uncertainty, processing-related impurities, and especially microstructural factors mask electronic effects. This is particularly evident when comparing the high-performing samples for Cu excess, Cr-, Co-, Ni-, and Zn-doped classes (stars in Figure 7), whose electronic structures are expected to be different.

Although several first-principles studies have examined how 3*d* transition-metal dopants modify the electronic structure of tetrahedrite,[23,43,47,50,130,131] a systematic comparison of their effects was lacking. Here, a comprehensive and consistent DFT analysis is presented for the most common Cu substitutions, namely Mn, Co, Fe, Ni and Zn.

Figure 8a shows the electronic band structure and element-projected density of states (PDOS) for undoped tetrahedrite at 0 K. Stoichiometric $Cu_{12}^{+}Sb_4^{3+}S_{12}^{2-}$ is intrinsically electron-deficient, resulting in partially occupied valence-band states. To relate the electronic structure to charge transport, the spatial distribution of these holes was analysed. The real-space charge density associated with valence-band states crossing the Fermi level (E_F) is uniform across symmetry-equivalent Cu sites, with no evidence of site-specific depletion or accumulation. Bader analysis using both PBE and SCAN functionals yields nearly identical charges for equivalent Cu atoms, confirming the absence of site-selective hole localisation. Furthermore, only a small charge difference is observed between Cu(1) 12*d* and Cu(2) 12*e*, reflecting their distinct coordination environments (Figure S6).[83]

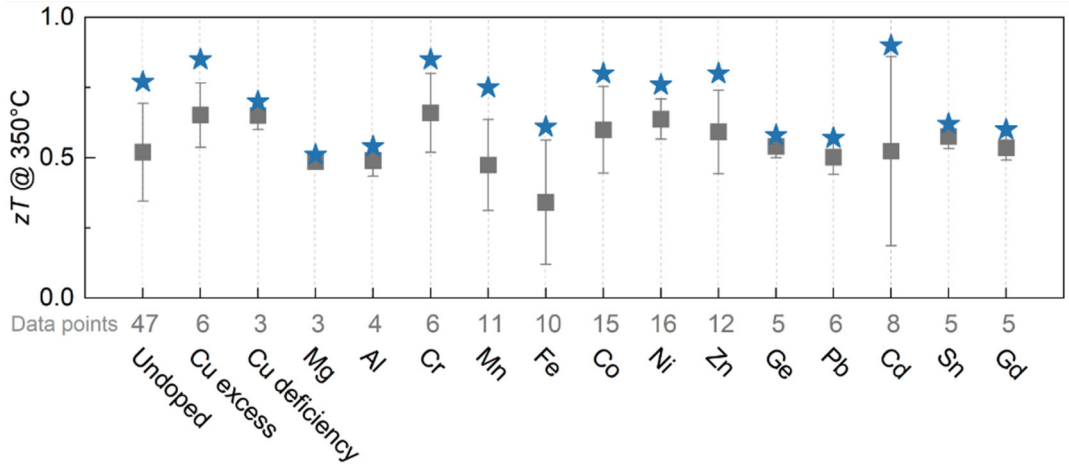

Figure 7. Average *zT* at 350 °C (squares) for undoped, Cu excess and deficiency conditions, and Cu-substituted tetrahedrites. Error bars represent standard deviations, and stars denote the highest value in each class (compositions and references provided in Table S1).[83] Co-doped compositions are excluded, and each class pools measurements across all doping levels. The number of data points is indicated below each class. The statistical analysis of dopant effects is presented in Table S2.[83]

Overall, these results confirm that holes are delocalised over the Cu–S network rather than associated with mixed Cu^{+}/Cu^{2+} valence at 12*d*. Accordingly, the valence band is dominated by Cu 3*d* – S 3*p* hybridisation, supporting hole delocalisation near the Fermi level and underpinning quasi-metallic transport.

Figure 8b to 8h presents the band structures and PDOS of $Cu_{12-x}M_xSb_4S_{13}$ ($x = 1$). In all cases, substitution at the 12*d* site is found to be energetically preferred. The electronic response to doping is governed by the energy and hybridisation of dopant *d* states relative to the valence-band edge, which control band dispersion and thus μ. The dopants fall into three regimes of increasing perturbation of the undoped electronic structure (Figure 8a).

In the weak perturbation regime (Zn, Mn), the valence-band edge remains largely unchanged. Zn adopts a closed-shell $3d^{10}$ configuration, placing its *d* states deep in the valence region, resulting in negligible hybridisation with valence states near the Fermi level. Consequently, band dispersion and high μ are preserved (Figure 8b). The fully occupied shell also leads to identical spin-up and spin-down PDOS, reflecting the absence of exchange splitting. Mn introduces a partially filled *d* shell and spin polarisation; however, its states remain sufficiently removed from the valence-band edge and weakly hybridised, leaving the dispersive valence bands near the Fermi level largely intact (Figure 8c).

In the moderate perturbation regime (Ni, Co), dopant d states lie closer to the Fermi level and hybridise with the Cu–S network, leading to noticeable but non-disruptive modifications of band dispersion. Ni induces moderate distortion of the valence band, while Co produces a slightly stronger restructuring and increased density of states near the Fermi level. In both cases, spin-dependent features arise from partially filled *d* shells, but the bands remain sufficiently dispersive to sustain carrier transport (Figure 8d and 8e).

In the strong perturbation regime (Fe), the electronic structure is markedly altered. Fe-derived *d* states appear at the valence-band edge, forming a weakly dispersive band intersecting the Fermi level (Figure 8f). The reduced dispersion and weak hybridisation indicate increased localisation, causing holes to occupy less delocalised orbitals. This enhances carrier scattering and disrupts transport pathways. The pronounced spin asymmetry reflects the partially filled $3d^6$ configuration and strong exchange splitting, leading to the most localised electronic behaviour among the dopants. This mechanism accounts for the experimentally observed reduction in σ for higher Fe concentrations).[33,77,100,132]

These calculations reveal that TE transport is governed by the degree of dopant–host hybridisation near the valence-band edge. Strong hybridisation preserves band dispersion and μ, whereas weakly hybridised states promote localisation and carrier scattering. Dopant–host hybridisation thus emerges as a unifying descriptor for the diverse transport behaviour reported across tetrahedrites.[133–136] Finally, tetrahedrite exhibits temperature-dependent behaviour; a Jahn–Teller-driven structural transition of the Cu sublattice has been reported at low temperature,[37] modifying the electronic states near the Fermi level. This suggests that hole distribution and transport evolve with temperature, and that a complete description requires coupling between electronic structure, lattice dynamics and structural distortions.

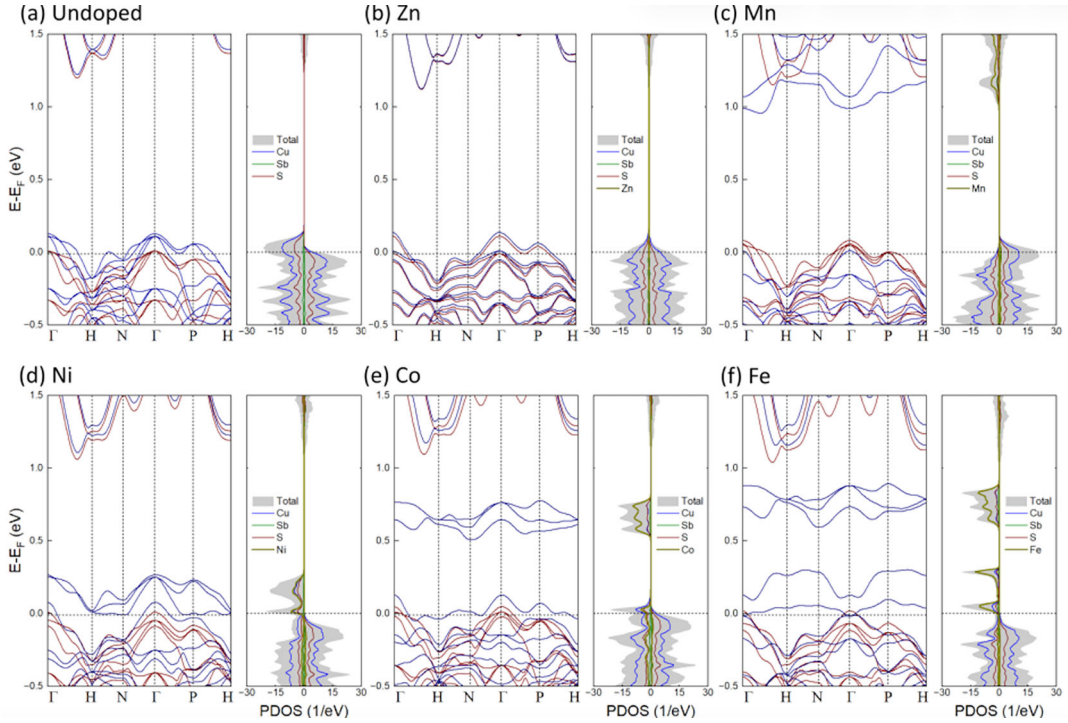

Figure 8. Spin-polarized electronic band structures and element-projected densities of states (PDOS), illustrating the progressive perturbation of the valence-band edge across the dopants. (a) undoped tetrahedrite and Cu12–xMxSb4S13 with x = 1 and M being (b) Zn, (c) Mn, (d) Ni, (e) Co and (f) Fe at Cu-12d. The PDOS highlights the increasing contribution of dopant *d* states near the valence-band edge across the series. In the band structures, blue and red lines correspond to spin-up-like and spin-down-like states, respectively, whereas in the PDOS positive and negative values represent spin-up and spin-down contributions.

While the DFT calculations were restricted to x = 1—owing to the large supercells required for more dilute substitution and the configurational complexity arising from multiple dopant arrangements at higher substitution levels—they provide a clear framework for interpreting concentration-dependent transport properties. Thus, the DFT results support the statistical finding that Fe is electronically distinct, while also demonstrating why dopant identity alone cannot explain the broader TE performance dispersion.

The influence of dopant concentration for $0< x \leq 2$ on the measured σ, K and S was examined for Ni, which offers the largest dataset ($N = 16$), and for Fe and Zn, which are of particular interest due to their natural occurrence in mineral tetrahedrite (Figure 9). Despite the limited datasets, discernible trends emerge: increasing dopant concentration generally reduces both σ and K for all three elements, whereas S increases nearly monotonically for Ni and exhibits apparent maxima for Fe and Zn (Figure 9). The corresponding zT values are shown in Figure 10, with high-performing data points highlighted by stars.

Doping with Ni yields consistently higher σ than the other elements across $0 \leq x \leq 2$ (Figure 9), indicating a more favourable balance between n and μ. This behaviour is consistent with the DFT results, where Ni belongs to the moderate perturbation regime and preserves relatively dispersive valence-band states. The resulting stability of zT over the full substitution range suggests that the modest reduction in μ is compensated by sustained enhancement in S and moderate suppression of K (Figure 10a).

Since Zn has a fully filled 3*d* shell, it acts primarily as a charge-compensating dopant, reducing hole concentration and shifting the Fermi level deeper into the band gap as concentration increases. This behaviour aligns with the weak perturbation regime identified from DFT, where the Cu–S-derived valence band remains largely unchanged. Up to $x = 1$, the reduction in σ is relatively modest and is offset by decreases in K and increases in S, yielding zT values comparable to or slightly exceeding those of undoped tetrahedrite (Figure 10b). At higher substitution levels, however, the strong reduction in n and the accompanying decline in S lead to suppressed zT, with the system approaching insulating behaviour at $x = 2$.[24]

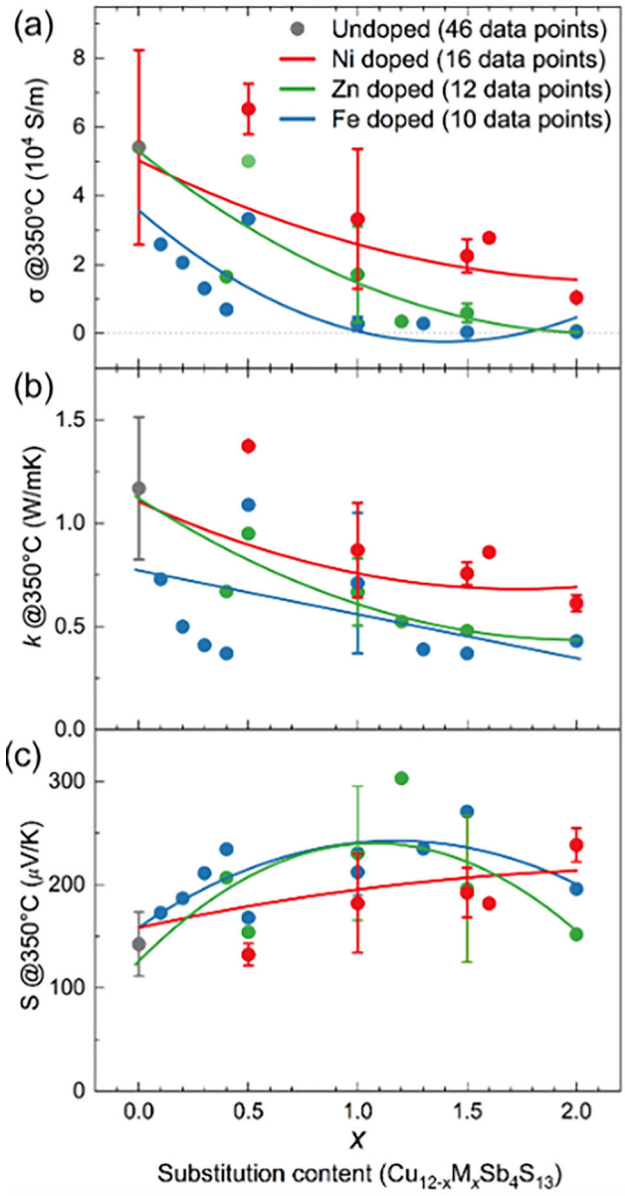

Figure 9. Effect of Ni-, Zn- and Fe-doping on the average transport properties. (a) electrical conductivity, (b) thermal conductivity and (c) Seebeck coefficient measured at 350 °C. Values at $x = 0$ correspond to the undoped composition (grey circles representing 46 data points). Error bars correspond to the standard deviation. Co-doping data are excluded. Parabolic fits were added to guide the eye.

Fe exhibits markedly different behaviour, consistent with its classification in the strong perturbation regime identified by DFT. Experimental studies indicate a concentration-dependent oxidation state, with Fe^{3+} dominating at low substitution levels ($0 \leq x \leq 1$) and increasing contributions from Fe^{2+} at higher concentrations.[34,137] At high Fe content, mixed valence states enable electron hopping between Fe sites.[138] The increasing activation energy for this process contributes to the suppression of σ with increasing Fe content.[139] This behaviour is consistent with the DFT results, which show that Fe introduces weakly dispersive states at the valence-band edge, promoting localisation. Even at low substitution levels, this perturbation induces a pronounced reduction in σ. For $x \leq 0.5$, the decrease in κ and enhancement in S partially compensate for this effect, maintaining zT comparable to undoped samples. At higher substitution levels, however, increased localisation and carrier scattering lead to substantial degradation of TE performance (Figure 10c).

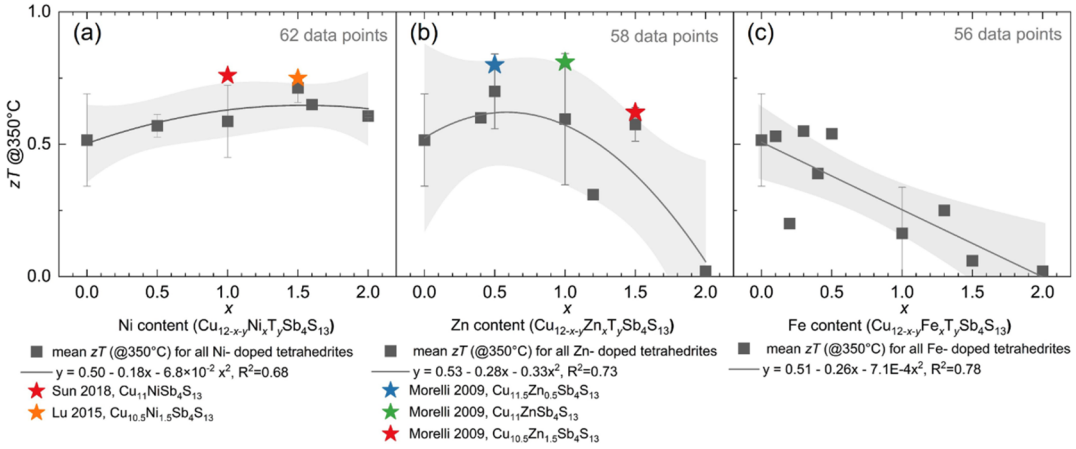

Figure 10. Average *zT* values at 350 °C. (a) Ni-, (b) Zn- and (c) Fe-doped samples. Error bars correspond to standard deviation. Co-doped samples are excluded. The undoped material corresponds to 38 data points (at $x = 0$). The curves represent parabolas fitted to the points, with 95% confidence intervals shown in grey. Stars highlight individual values identified below the plots.

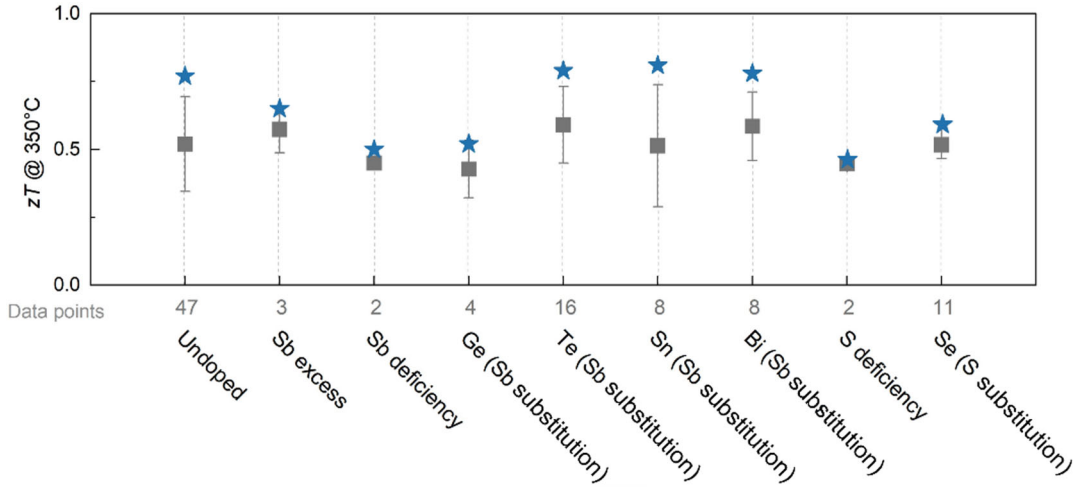

Figure 11. Average *zT* at 350 °C (squares) for undoped, Sb excess and deficiency, and S deficiency conditions, and Sb- and S-substituted tetrahedrites. The error bars correspond to the standard deviation. The stars correspond to the highest value in each set, with details and references provided in Table S1.[83] Co-doped compositions are excluded, and each class pools measurements across all doping levels. The number of data points is indicated below each class. The statistical analysis of dopant effects is presented in Table S2.[83]

Antimony and sulphur substitution

Substitution at the Sb sublattice remains comparatively underexplored relative to the extensively studied Cu-site chemistry. Yet such substitutions are intrinsically relevant: natural tetrahedrites commonly incorporate elements such as As, Bi, and Te on Sb positions, reflecting a broad geochemical tolerance.[140] Understanding how these substitutions influence TE performance is therefore essential for guiding compositional optimisation.

Figure 11 presents the average *zT* values for Sb-substituted tetrahedrites together with those of S-substituted materials, excluding co-doped compositions to isolate single-dopant effects. Statistical analysis using the Mann–Whitney *U* test shows no significant difference between either Sb or S substitutions and undoped tetrahedrite (Table S2),[83] indicating that any dopant-induced trends are masked by the scatter inherent to the limited dataset, the pooling of mixed concentrations within each class, and processing-induced variations.

Among Sb-site dopants, Te consistently yields high *zT* values (above 0.7).[133,141,142] This behaviour can be rationalised by Te^{4+} substituting for Sb^{3+}, with the excess electrons lowering the hole concentration, which enhances *S*.[141,143] Bismuth

substitution[120,140] is nominally isovalent with Sb, but the possible presence of Bi^{5+} may similarly donate electrons, producing comparable reductions in hole concentration and corresponding increases in *S*.[140]

Substitution of sulphur has been investigated even less thoroughly.[144–147] Although both the 24*g* and 2*a* sites have been proposed as viable substitutional positions,[141] systematic studies are lacking, and S substitution is typically introduced indirectly as part of broader doping strategies.[118,148]

Overall, neither Sb nor S substitutions produce statistically significant changes in zT. However, several Sb-site dopants exhibit small but discernible effect sizes in the Mann–Whitney analysis, whereas S substitution shows no measurable influence within the available data, and its independent contribution to TE performance remains unclear.

Challenges in Hall effect measurements

Accurate determination of n and μ is essential for understanding the effects of doping, particularly when comparing different dopant species and substitution levels. However, obtaining reliable Hall effect data in these materials remains a significant experimental challenge. Numerous studies report Hall measurements as unreliable or inconclusive,[23,43,63,112,116,117,149,150] and even when n and μ values are published, they are often accompanied by large uncertainties and require extensive averaging over repeated measurements.[147,151] These difficulties arise from the relatively low μ in tetrahedrites, combined with microstructural complexity—such as porosity—which further reduces the measurable Hall voltage and increases susceptibility to artefacts.

Consequently, the underlying electrical transport mechanisms remain poorly resolved,[151] hindering direct verification of n inferred from electronic-structure analysis and complicating quantitative comparison with theoretical predictions. Most Hall measurements are performed in the van der Pauw geometry, where the Hall voltages are extremely small and easily obscured by spurious Seebeck voltages generated by minute temperature gradients across the sample. More robust strategies are therefore required to obtain reliable values of n; these include low-temperature measurements, which suppress TE parasitic voltages, as well as AC Hall techniques, which can distinguish genuine Hall signals from thermally induced contributions.[152]

Conclusions

Tetrahedrites represent a promising class of p-type TE materials owing to their natural abundance, low toxicity, and intrinsically favourable transport properties. However, chemical optimisation in this system has been hindered by the large scatter in reported TE performance, which confounds clear optimisation strategies. To address this, a comprehensive meta-analysis of published transport data was performed, aggregating more than 6,000 TE property data points.

The meta-analysis reveals substantial variability in reported performance, underscoring the absence of clear optimisation pathways. Despite this variability, compositional trends emerged: moderate Cu substitution ($x < 1$) generally enhances zT through increased S and reduced κ, whereas higher substitution levels typically suppress σ and degrade overall performance. However, dopant identity is not the primary determinant of TE performance. Across most dopants, peak zT values vary only modestly, with Fe representing a notable exception due to its tendency to produce highly resistive samples. Instead, the analysis indicates that densification quality and microstructural features exert a stronger influence on zT than dopant chemistry at the present stage of material development.

The present findings indicate that the large variability reported in tetrahedrite performance arises primarily from differences in processing rather than composition. Advancing this material system therefore requires a shift in emphasis from compositional exploration toward improved control over consolidation, microstructure, and measurement reproducibility. Establishing standardised processing protocols together with quantitative correlations between microstructure and transport properties will be critical to fully realise the potential of tetrahedrites as sustainable TE materials.

Ethics and consent

Ethical approval and consent were not required.

Data availability

Source data

The datasets compiled in this work are available at the ZENODO repository: Tetrahedrites for Thermoelectric Applications: A database. https://doi.org/10.5281/zenodo.17692053.[60] Table 1 presents the TE properties measured at 350 °C for each composition along with the references. Supplementary materials referenced in the paper are available at the ZENODO repository: Supplementary Materials for Hidden processing drivers of thermoelectric performance in tetrahedrites. https://doi.org/10.5281/zenodo.20449220.[83]

Table 1. Thermoelectric properties of tetrahedrites at 350 °C.

Composition	*zT*	*S* μV/K	σ S/m	κ W/(mK)	*D* %	Ref.	Composition	*zT*	*S* μV/K	σ S/m	κ W/(mK)	*D* %	Ref.
Undoped													
$Cu_{12}Sb_4S_{13}$	0.45	122.7	2.27	-	98	23	$Cu_{12}Sb_4S_{13}$	-	-	-	-	96	127
$Cu_{12}Sb_4S_{13}$	0.49	121.3	7.69	1.48	98	24	$Cu_{12}Sb_4S_{13}$	0.69	173.0	3.00	0.80	99	128
$Cu_{12}Sb_4S_{13}$	-	-	-	-	75	33	$Cu_{12}Sb_4S_{13}$	0.49	122.9	7.17	1.46	95	129
$Cu_{12}Sb_4S_{13}$	0.64	122.5	10.00	1.37	-	43	$Cu_{12}Sb_4S_{13}$	0.76	137.0	9.09	1.37	95	134
$Cu_{12}Sb_4S_{13}$	0.64	145.0	6.80	1.37	95	47	$Cu_{12}Sb_4S_{13}$	0.43	110.0	8.40	1.52	96	136
$Cu_{12}Sb_4S_{13}$	0.70	-	-	-	98	48	$Cu_{12}Sb_4S_{13}$	0.77	127.0	8.33	1.16	90	140
$Cu_{12}Sb_4S_{13}$	0.02	138.0	0.19	0.65	93	77	$Cu_{12}Sb_4S_{13}$	0.46	116.0	7.10	1.45	98	141
$Cu_{12}Sb_4S_{13}$	0.44	114.0	8.40	1.54	96	96	$Cu_{12}Sb_4S_{13}$	0.39	122.0	7.20	1.72	98	143
$Cu_{12}Sb_4S_{13}$	0.15	160.0	0.50	0.38	94	97	$Cu_{12}Sb_4S_{13}$	0.46	122.0	7.14	1.46	-	144
$Cu_{12}Sb_4S_{13}$	-	-	-	-	88	100	$Cu_{12}Sb_4S_{13}$	0.30	119.0	3.20	0.96	86	145
$Cu_{12}Sb_4S_{13}$	0.54	135.0	5.26	1.20	98	102	$Cu_{12}Sb_4S_{13}$	0.44	110.0	8.80	1.60	96	146
$Cu_{12}Sb_4S_{13}$	0.76	130.0	10.50	1.32	95	103	$Cu_{12}Sb_4S_{13}$	0.61	122.0	6.80	0.99	99	148
$Cu_{12}Sb_4S_{13}$	0.69	175.0	3.00	0.82	-	106	$Cu_{12}Sb_4S_{13}$	0.69	175.0	2.90	0.80	99	153
$Cu_{12}Sb_4S_{13}$	0.64	155.0	3.80	0.95	-	106	$Cu_{12}Sb_4S_{13}$	0.43	122.3	7.14	1.49	98	154
$Cu_{12}Sb_4S_{13}$	0.62	150.0	3.90	0.92	-	106	$Cu_{12}Sb_4S_{13}$	0.42	120.0	7.14	1.45	95	155
$Cu_{12}Sb_4S_{13}$	0.60	170.0	2.90	0.90	-	106	$Cu_{12}Sb_4S_{13}$	0.60	245.0	0.91	0.55	95	156
$Cu_{12}Sb_4S_{13}$	0.50	194.0	1.89	0.80	99	107	$Cu_{12}Sb_4S_{13}$	0.61	245.0	1.00	0.58	95	156
$Cu_{12}Sb_4S_{13}$	0.55	154.4	4.42	1.11	95	109	$Cu_{12}Sb_4S_{13}$	0.80	155.0	5.50	0.93	99	157
$Cu_{12}Sb_4S_{13}$	0.48	136.0	5.23	1.21	95	109	$Cu_{12}Sb_4S_{13}$	0.69	176.0	3.00	0.77	99	158
$Cu_{12}Sb_4S_{13}$	0.45	134.5	4.99	1.24	95	109	$Cu_{12}Sb_4S_{13}$	0.70	167.0	3.60	0.90	99	158
$Cu_{12}Sb_4S_{13}$	0.40	127.8	5.19	1.28	95	109	$Cu_{12}Sb_4S_{13}$	0.60	186.0	2.30	0.80	99	155
$Cu_{12}Sb_4S_{13}$	0.39	128.3	5.08	1.32	95	109	$Cu_{12}Sb_4S_{13}$	0.42	120.0	8.00	1.74	97	159
$Cu_{12}Sb_4S_{13}$	0.41	125.0	8.00	1.73	96	113	$Cu_{12}Sb_4S_{13}$	0.48	123.0	7.60	1.49	95	160
$Cu_{12}Sb_4S_{13}$	0.44	113.0	8.30	1.50	96	118	$Cu_{12}Sb_4S_{13}$	0.69	125.0	7.50	0.99	-	161
$Cu_{12}Sb_4S_{13}$	0.00	140.0	0.00	1.15	95	119	$Cu_{12}Sb_4S_{13}$	0.50	125.0	7.75	1.40	95	162
Cu deficiency													
$Cu_{11.9}Sb_4S_{13}$	0.70	155.0	4.10	0.82	99	128	$Cu_{11.7}Sb_4S_{13}$	0.60	150.0	4.50	1.00	99	128
$Cu_{11.8}Sb_4S_{13}$	0.65	155.0	3.50	0.82	99	128							
Cu excess													
$Cu_{12.1}Sb_4S_{13}$	0.60	194.0	1.50	0.60	99	128	$Cu_{13}Sb_4S_{13}$	0.67	163.0	2.46	0.59	95	129

Open Research Europe 2026, 6:221 Last updated: 20 OCT 2026

Table 1. *Continued*

Composition	*zT*	*S* μV/K	σ S/m	κ W/(mK)	*D* %	Ref.	Composition	*zT*	*S* μV/K	σ S/m	κ W/(mK)	*D* %	Ref.
$Cu_{12.2}Sb_4S_{13}$	0.68	204.0	1.50	0.60	99	128	$Cu_{13}Sb_4S_{12}Se$	0.78	142.4	5.59	0.91	95	129
$Cu_{12.3}Sb_4S_{13}$	-	-	-	-	96	127	$Cu_{13.5}Sb_4S_{13}$	-	-	-	-	96	127
$Cu_{12.3}Sb_4S_{13}$	0.60	208.0	1.30	0.60	99	128	$Cu_{13.5}Sb_4S_{13}$	0.85	180.0	2.09	0.48	95	129
$Cu_{12.5}Sb_4S_{13}$	0.51	136.0	3.52	0.81	95	129	$Cu_{13.5}Sb_4S_{12}Se$	0.80	159.7	3.77	0.76	95	129
$Cu_{12.5}Sb_4S_{12}Se$	0.76	124.0	7.13	0.89	95	129	$Cu_{14}Sb_4S_{13}$	-	-	-	-	96	127
$Cu_{13}Sb_4S_{13}$	-	-	-	-	96	127							
Al doping (Cu)													
$Cu_{11.9}Al_{0.1}Sb_4S_{13}$	0.54	121.5	6.80	1.19	96	115	$Cu_{11.5}Al_{0.5}Sb_4S_{13}$	0.47	126.4	5.30	1.12	95	115
$Cu_{11.75}Al_{0.25}Sb_4S_{13}$	0.53	122.3	6.60	1.18	96	115	$Cu_{11.25}Al_{0.75}Sb_4S_{13}$	0.42	130.2	4.48	1.10	94	115
Mg doping (Cu)													
$Cu_{11.5}Mg_{0.5}Sb_4S_{13}$	0.46	135.0	4.45	1.01	95	162	$Cu_{10.5}Mg_{1.5}Sb_4S_{13}$	0.51	160.0	2.33	0.72	95	162
$Cu_{11}MgSb_4S_{13}$	0.49	155.0	3.24	0.92	95	162							
Cr doping (Cu)													
$Cu_{11.85}Cr_{0.15}Sb_4S_{13}$	0.61	138.0	6.67	1.24	93	108	$Cu_{11.5}Cr_{0.5}Sb_4S_{13}$	0.70	155.0	5.00	1.05	93	108
$Cu_{11.75}Cr_{0.25}Sb_4S_{13}$	0.64	130.0	8.33	1.22	89	108	$Cu_{11.25}Cr_{0.75}Sb_4S_{13}$	0.73	167.0	3.23	0.82	95	108
$Cu_{11.65}Cr_{0.35}Sb_4S_{13}$	0.85	185.0	2.78	0.71	97	108	$Cu_{11}CrSb_4S_{13}$	0.43	167.0	3.23	0.82	94	108
Mn doping (Cu)													
$Cu_{11.5}Mn_{0.5}Sb_4S_{13}$	-	-	-	-	85	100	$Cu_{11}MnSb_4S_{13}$	0.48	170.0	1.80	0.65	94	101
$Cu_{11.5}Mn_{0.5}Sb_4S_{13}$	0.56	139.2	5.00	1.24	95	43	$Cu_{11}MnSb_4S_{13}$	0.33	264.0	0.42	0.53	97	107
$Cu_{11.5}Mn_{0.5}Sb_4S_{13}$	0.75	142.0	4.50	0.76	-	161	$Cu_{10.6}Mn_{1.4}Sb_4S_{13}$	0.34	230.0	0.77	0.78	95	134
$Cu_{11.1}Mn_{0.9}Sb_4S_{13}$	0.46	167.0	2.95	1.10	95	134	$Cu_{10.5}Mn_{1.5}Sb_4S_{13}$	-	-	-	-	85	100
$Cu_{11.6}Mn_{0.4}Sb_4S_{13}$	0.56	135.0	6.17	1.22	95	134	$Cu_{10.2}Mn_{1.8}Sb_4S_{13}$	0.18	330.0	0.15	0.62	98	134
$Cu_{11}MnSb_4S_{13}$	-	-	-	-	85	100	$Cu_{10}Mn_2Sb_4S_{13}$	-	-	-	-	75-80	33
$Cu_{11}MnSb_4S_{13}$	0.59	215.0	1.10	0.54	-	161	$Cu_{10}Mn_2Sb_4S_{13}$	-	-	-	-	88	100
$Cu_{11}MnSb_4S_{13}$	0.61	175.0	2.20	0.68	96	101	$Cu_{10}Mn_2Sb_4S_{13}$	0.35	332.0	0.20	0.32	-	161
Fe doping (Cu)													
$Cu_{11.9}Fe_{0.1}Sb_4S_{13}$	0.53	172.8	2.59	0.87	99	110	$Cu_{11}FeSb_4S_{13}$	0.36	235.0	0.50	0.48	93	132
$Cu_{11.8}Fe_{0.2}Sb_4S_{13}$	0.61	187.0	2.06	0.72	100	110	$Cu_{10}FeZnSb_4S_{13}$	0.03	212.0	0.10	1.10	95	119
$Cu_{11.8}Fe_{0.2}Sb_4S_{13}$	-	-	-	-	98	154	$Cu_{10.7}Fe_{1.3}Sb_4S_{13}$	0.25	235.0	0.29	0.39	93	132
$Cu_{11.7}Fe_{0.3}Sb_4S_{13}$	0.55	211.4	1.31	0.65	100	110	$Cu_{10.5}Fe_{1.5}Sb_4S_{13}$	0.06	271.0	0.04	0.37	87	77
$Cu_{11.6}Fe_{0.4}Sb_4S_{13}$	0.39	234.6	0.70	0.61	98	110	$Cu_{10}Fe_2Sb_4S_{13}$	-	-	-	-	75-80	33
$Cu_{11.5}Fe_{0.5}Sb_4S_{13}$	0.54	168.3	3.33	1.09	95	43	$Cu_{10}Fe_2Sb_4S_{13}$	0.02	196.0	0.04	0.43	85	77

Open Research Europe 2026, 6:221 Last updated: 20 OCT 2026

Table 1. *Continued*

Composition	*zT*	*S* μV/K	σ S/m	κ W/(mK)	*D* %	Ref.	Composition	*zT*	*S* μV/K	σ S/m	κ W/(mK)	*D* %	Ref.
$Cu_{11.5}Fe_{0.5}Sb_4S_{13}$	-	-	-	-	98	154	$Cu_{10}Fe_2Sb_4S_{13}$	-	-	0.01	0.20	85	100
$Cu_{11}FeSb_4S_{13}$	0.10	190.0	0.24	0.55	98	107							
Co doping (Cu)													
$Cu_{11.8}Co_{0.2}Sb_4S_{13}$	0.73	171.5	3.10	0.76	99	163	$Cu_{11}CoSb_4S_{13}$	0.71	187.0	3.27	1.03	95	56
$Cu_{12.18}Co_{0.25}Sb_{3.68}Te_{0.62}S_{13}$	0.55	145.0	5.20	0.93	92	150	$Cu_{11}CoSb_4S_{13}$	0.34	290.0	0.35	0.55	98	107
$Cu_{11.88}Co_{0.32}Sb_{3.11}Te_{1.05}S_{13}$	0.58	180.0	2.55	0.76	92	150	$Cu_{11}CoSb_4S_{13}$	0.51	251.8	0.80	0.58	98	163
$Cu_{11.6}Co_{0.4}Sb_4S_{13}$	0.59	191.0	2.10	0.80	98	163	$Cu_{10.7}Co_{1.3}Sb_4S_{13}$	0.64	171.7	2.12	0.68	92	150
$Cu_{11.67}Co_{0.47}Sb_{3.36}Te_{0.77}S_{13}$	0.57	170.0	3.10	0.77	92	150	$Cu_{10.5}Co_{1.5}Sb_4S_{13}$	0.72	230.0	1.71	0.72	95	150
$Cu_{11.5}Co_{0.5}Sb_4S_{13}$	0.79	157.2	6.00	1.24	98	43	$Cu_{10.49}Co_{1.51}Sb_4S_{13}$	0.59	199.3	1.51	0.60	92	150
$Cu_{11.5}Co_{0.5}Sb_4S_{13}$	0.80	158.0	6.25	1.25	95	56	$Cu_{10.3}Co_{1.7}Sb_4S_{13}$	0.56	219.0	0.94	0.53	92	150
$Cu_{11.4}Co_{0.6}Sb_4S_{13}$	0.61	198.9	1.90	0.74	98	163	$Cu_{10}Co_2Sb_4S_{13}$	-	-	-	-	75-80	33
$Cu_{11.2}Co_{0.8}Sb_4S_{13}$	0.50	234.1	0.90	0.62	97	163	$Cu_{10}Co_2Sb_4S_{13}$	0.25	288.0	0.27	0.62	95	56
$Cu_{11.47}Co_{0.82}Sb_{3.78}Te_{0.41}S_{13}$	0.69	175.0	6.10	0.81	92	150	$Cu_{10}Co_2Sb_4S_{13}$	-	-	-	-	85	100
$Cu_{11.1}Co_{0.9}Sb_4S_{13}$	0.65	157.0	3.00	0.76	92	150							
Ni doping (Cu)													
$Cu_{11.5}Ni_{0.5}Sb_4S_{13}$	0.54	125.0	7.04	1.37	96	96	$Cu_{10}NiZnSb_4S_{13}$	0.52	250.0	0.66	0.50	95	156
$Cu_{11.5}Ni_{0.5}Sb_4S_{13}$	0.55	140.0	6.00	1.38	98	105	$Cu_{10}NiZnSb_4S_{13}$	0.45	200.0	1.10	0.63	95	156
$Cu_{10.5}Ni_{0.5}ZnSb_4S_{13}$	0.62	220.0	1.06	0.50	98	130	$Cu_{10.5}Ni_{1.3}Zn_{0.2}Sb_4S_{13}$	0.78	188.0	2.43	0.70	98	130
$Cu_{10}Ni_{0.5}Zn_{1.5}Sb_4S_{13}$	0.34	320.0	0.22	0.41	95	156	$Cu_{10.5}Ni_{1.5}Sb_4S_{13}$	0.65	177.0	2.50	0.81	96	96
$Cu_{10}Ni_{0.5}Zn_{1.5}Sb_4S_{13}$	0.39	275.0	0.35	0.48	95	156	$Cu_{10.5}Ni_{1.5}Sb_4S_{13}$	0.74	220.0	1.70	0.70	98	105
$Cu_{11}NiSb_4S_{13}$	0.68	167.8	5.00	1.06	89	43	$Cu_{10.5}Ni_{1.5}Sb_4S_{13}$	0.67	180.0	2.56	0.76	98	130
$Cu_{11}NiSb_4S_{13}$	0.61	150.0	4.60	1.08	96	96	$Cu_{10}Ni_{1.5}Zn_{0.5}Sb_4S_{13}$	0.51	215.0	1.25	0.68	95	156
$Cu_{11}NiSb_4S_{13}$	0.56	215.0	1.20	0.65	93	97	$Cu_{10}Ni_{1.5}Zn_{0.5}Sb_4S_{13}$	0.55	220.0	1.10	0.58	95	156
$Cu_{11}NiSb_4S_{13}$	0.76	165.0	4.00	0.90	98	105	$Cu_{10.4}Ni_{1.6}Sb_4S_{13}$	0.65	182.0	2.78	0.86	98	102
$Cu_{11}NiSb_4S_{13}$	0.36	265.0	0.40	0.53	98	107	$Cu_{10}Ni_2Sb_4S_{13}$	-	-	-	-	75-80	33
$Cu_{11}NiSb_4S_{13}$	0.55	135.0	4.85	1.00	95	160	$Cu_{10}Ni_2Sb_4S_{13}$	0.58	216.0	1.20	0.67	96	96
$Cu_{10.5}NiZn_{0.5}Sb_4S_{13}$	0.44	321.0	0.25	0.40	91	97	$Cu_{10}Ni_2Sb_4S_{13}$	-	-	-	-	85	100
$Cu_{10.5}NiZn_{0.5}Sb_4S_{13}$	0.84	200.0	2.05	0.58	98	134	$Cu_{10}Ni_2Sb_4S_{13}$	0.61	254.0	1.00	0.60	98	105
$Cu_{10.2}NiZn_{0.7}Sb_4S_{13}$	0.32	320.0	0.16	0.39	90	97							
Zn doping (Cu)													
$Cu_{11.075}Zn_{0.025}Sb_4S_{12.8}Se_{0.2}$	0.54	122.0	9.00	1.41	97	146	$Cu_{11}ZnSb_4S_{13}$	0.70	182.0	3.13	0.88	98	23
$Cu_{11.95}Zn_{0.05}Sb_4S_{12.8}Se_{0.2}$	0.65	135.0	8.00	1.34	96	146	$Cu_{11}ZnSb_4S_{13}$	0.63	202.1	2.00	0.77	90	43

Open Research Europe 2026, 6:221 Last updated: 20 OCT 2026

Table 1. *Continued*

Composition	*zT*	*S* μV/K	σ S/m	κ W/(mK)	*D* %	Ref.	Composition	*zT*	*S* μV/K	σ S/m	κ W/(mK)	*D* %	Ref.
$Cu_{11.025}Zn_{0.075}Sb_4S_{12.8}Se_{0.2}$	0.63	130.0	7.50	1.37	96	146	$Cu_{11}ZnSb_4S_{13}$	0.24	305.0	0.20	0.48	98	107
$Cu_{11.9}Zn_{0.1}Sb_4S_{12.8}Se_{0.2}$	0.49	120.0	7.60	1.38	97	146	$Cu_{11}ZnSb_4S_{13}$	0.81	184.7	2.94	0.75	98	154
$Cu_{11.9}Zn_{0.1}Sb_{3.9}Bi_{0.1}S_{13}$	0.55	177.0	2.50	0.87	99	112	$Cu_{10}FeZnSb_4S_{13}$	0.03	212.0	0.10	1.10	95	119
$Cu_{11.9}Zn_{0.1}Sb_{3.8}Bi_{0.2}S_{13}$	0.51	160.0	2.90	0.97	99	112	$Cu_{10}NiZnSb_4S_{13}$	0.45	200.0	1.10	0.63	95	156
$Cu_{11.8}Zn_{0.2}Sb_{3.8}Bi_{0.2}S_{13}$	0.50	225.0	0.90	0.58	99	112	$Cu_{10}NiZnSb_4S_{13}$	0.52	250.0	0.66	0.50	95	156
$Cu_{11.8}Zn_{0.2}Sb_{3.6}Bi_{0.4}S_{13}$	0.42	190.0	1.20	0.67	99	112	$Cu_{10.8}Zn_{1.2}Sb_4S_{13}$	0.31	303.0	0.35	0.53	99	153
$Cu_{10.5}Ni_{1.3}Zn_{0.2}Sb_4S_{13}$	0.78	188.0	2.43	0.70	98	130	$Cu_{10.5}Zn_{1.5}Sb_4S_{13}$	0.06	146.0	0.15	0.40	83	77
$Cu_{11.6}Zn_{0.4}Sb_4S_{13}$	0.60	207.0	1.65	0.67	97	153	$Cu_{10.5}Zn_{1.5}Sb_4S_{13}$	-	-	-	-	98	164
$Cu_{10.5}NiZn_{0.5}Sb_4S_{13}$	0.44	321.0	0.25	0.40	91	97	$Cu_{10}Ni_{0.5}Zn_{1.5}Sb_4S_{13}$	0.34	320.0	0.22	0.41	95	156
$Cu_{10.5}NiZn_{0.5}Sb_4S_{13}$	0.84	200.0	2.05	0.58	98	130	$Cu_{10}Ni_{0.5}Zn_{1.5}Sb_4S_{13}$	0.39	275.0	0.35	0.48	95	156
$Cu_{10}Ni_{1.5}Zn_{0.5}Sb_4S_{13}$	0.51	215.0	1.25	0.68	95	156	$Cu_{10.5}Zn_{1.5}Sb_4S_{13}$	0.53	246.0	0.81	0.57	98	23
$Cu_{10}Ni_{1.5}Zn_{0.5}Sb_4S_{13}$	0.55	220.0	1.10	0.58	95	156	$Cu_{10.5}Zn_{1.5}Sb_4S_{13}$	0.62	246.2	0.79	0.48	98	154
$Cu_{11.5}Zn_{0.5}Sb_4S_{13}$	0.60	137.0	6.00	1.20	98	23	$Cu_{10}Zn_2Sb_4S_{13}$	-	-	-	-	75-80	33
$Cu_{11.5}Zn_{0.5}Sb_4S_{13}$	0.80	154.1	5.00	0.95	98	43	$Cu_{10}Zn_2Sb_4S_{13}$	0.02	152.0	0.07	0.43	87	77
$Cu_{10.2}NiZn_{0.7}Sb_4S_{13}$	0.32	320.0	0.16	0.39	90	97	$Cu_{10}Zn_2Sb_4S_{13}$	-	-	-	-	88	100
$Cu_{11.2}Zn_{0.8}Sb_4S_{13}$	0.48	223.0	0.98	0.69	99	153							
Ga doping (Cu)													
$Cu_{11.9}Ga_{0.1}Sb_{3.85}Te_{0.15}S_{14}$	0.52	149.0	5.10	1.38	98	143	$Cu_{11.7}Ga_{0.3}Sb_{3.55}Te_{0.45}S_{15}$	0.67	190.0	2.80	0.85	98	143
$Cu_{11.8}Ga_{0.2}Sb_{3.7}Te_{0.3}S_{13}$	0.80	175.0	4.20	0.96	98	143							
Ge doping (Cu)													
$Cu_{11.9}Ge_{0.1}Sb_4S_{13}$	0.50	125.0	6.50	1.28	96	155	$Cu_{11.5}Ge_{0.5}Sb_4S_{13}$	0.54	182.0	1.47	0.55	90	155
$Cu_{11.7}Ge_{0.3}Sb_4S_{13}$	0.58	158.0	2.80	0.75	97	155	$Cu_{11.4}Ge_{0.6}Sb_4S_{13}$	0.50	215.0	0.82	0.49	94	155
$Cu_{11.6}Ge_{0.4}Sb_4S_{13}$	0.58	148.0	4.20	1.02	93	155							
Cd doping (Cu)													
$Cu_{11.75}Cd_{0.25}Sb_4S_{13}$	0.60	132.0	8.33	1.40	92	103	$Cu_{10.75}Cd_{1.25}Sb_4S_{13}$	0.57	215.0	1.61	0.82	87	103
$Cu_{11.5}Cd_{0.5}Sb_4S_{13}$	0.84	150.0	5.26	0.90	92	103	$Cu_{10.5}Cd_{1.5}Sb_4S_{13}$	0.02	134.0	0.08	0.51	85	77
$Cu_{11.25}Cd_{0.75}Sb_4S_{13}$	0.90	155.0	4.54	0.72	85	103	$Cu_{10.5}Cd_{1.5}Sb_4S_{13}$	0.52	255.0	0.87	0.65	80	103
$Cu_{11}CdSb_4S_{13}$	0.72	185.0	2.86	0.85	93	103	$Cu_{10}Cd_2Sb_4S_{13}$	0.02	129.0	0.05	0.29	89	77
In doping (Cu)													
$Cu_{11.975}In_{0.025}Sb_4S_{12.8}Se_{0.2}$	0.69	120.0	8.80	1.15	95	118	$Cu_{11.925}In_{0.075}Sb_4S_{12.8}Se_{0.2}$	0.61	126.0	7.50	1.22	96	118
$Cu_{11.95}In_{0.05}Sb_4S_{12.8}Se_{0.2}$	0.72	122.0	8.40	1.11	96	118							

Table 1. *Continued*

Composition	*zT*	*S* μV/K	σ S/m	κ W/(mK)	*D* %	Ref.	Composition	*zT*	*S* μV/K	σ S/m	κ W/(mK)	*D* %	Ref.
Sn doping (Cu)													
$Cu_{11.9}Sn_{0.1}Sb_4S_{13}$	0.53	130.0	6.66	1.28	93	155	$Cu_{11.5}Sn_{0.5}Sb_4S_{13}$	0.60	193.0	1.50	0.61	96	155
$Cu_{11.7}Sn_{0.3}Sb_4S_{13}$	0.60	150.0	4.10	1.00	98	155	$Cu_{11.4}Sn_{0.6}Sb_4S_{13}$	0.53	240.0	0.74	0.52	98	155
$Cu_{11.6}Sn_{0.4}Sb_4S_{13}$	0.62	171.0	2.43	0.73	95	155							
Pb doping (Cu)													
$Cu_{11.75}Pb_{0.25}Sb_4S_{13}$	0.52	132.2	5.65	1.20	98	159	$Cu_{11}PbSb_4S_{13}$	0.57	181.7	1.90	0.68	99	159
$Cu_{11.5}Pb_{0.5}Sb_4S_{13}$	0.56	146.3	4.40	1.09	99	159	$Cu_{10.75}Pb_{1.25}Sb_4S_{13}$	0.50	194.2	1.45	0.68	99	159
$Cu_{11.25}Pb_{0.75}Sb_4S_{13}$	0.44	160.0	2.55	1.00	96	159	$Cu_{10.5}Pb_{1.5}Sb_4S_{13}$	0.42	237.2	0.75	0.69	99	159
Gd doping (Cu)													
$Cu_{11.95}Gd_{0.05}Sb_4S_{12.6}Se_{0.4}$	0.64	128.0	8.10	1.30	98	48	$Cu_{11.7}Gd_{0.3}Sb_4S_{13}$	0.60	118.0	9.00	1.46	96	136
$Cu_{11.9}Gd_{0.1}Sb_4S_{13}$	0.48	115.0	8.80	1.51	97	136	$Cu_{11.6}Gd_{0.4}Sb_4S_{13}$	0.55	118.0	8.70	1.40	96	136
$Cu_{11.9}Gd_{0.2}Sb_4S_{13}$	0.52	115.0	8.70	1.45	97	136	$Cu_{11.5}Gd_{0.5}Sb_4S_{13}$	0.53	120.0	8.30	1.45	96	136
Sb deficiency													
$Cu_{12}Sb_{3.8}S_{13}$	0.50	135.0	6.10	1.25	95	113	$Cu_{12}Sb_{3.9}S_{13}$	0.47	125.0	6.90	1.55	95	113
Sb excess													
$Cu_{12}Sb_{4.1}S_{13}$	0.59	125.0	9.00	1.42	97	113	$Cu_{12}Sb_{4.3}S_{13}$	0.48	134.0	6.50	1.46	97	113
$Cu_{12}Sb_{4.2}S_{13}$	0.65	135.0	7.40	1.24	95	113							
Ge doping (Sb)													
$Cu_{12}Sb_{3.6}Ge_{0.4}S_{13}$	0.40	224.0	0.55	0.60	98	117	$Cu_{12}Sb_{3.8}Ge_{0.2}S_{13}$	0.52	180.0	2.20	0.81	100	117
$Cu_{12}Sb_{3.7}Ge_{0.3}S_{13}$	0.29	200.0	1.20	0.72	99	117	$Cu_{12}Sb_{3.9}Ge_{0.1}S_{13}$	0.50	155.0	3.25	1.00	99	117
Sn doping (Sb)													
$Cu_{12}Sb_{3.9}Sn_{0.1}S_{13}$	0.50	170.0	2.40	0.87	99	116	$Cu_{12}Sb_{3.65}Sn_{0.35}S_{13}$	0.81	165.0	3.95	0.89	98	135
$Cu_{12}Sb_{3.8}Sn_{0.2}S_{13}$	0.44	175.0	1.80	0.85	100	116	$Cu_{12}Sb_{3.6}Sn_{0.4}S_{13}$	0.20	238.0	0.30	0.61	99	116
$Cu_{12}Sb_{3.75}Sn_{0.25}S_{13}$	0.80	155.0	4.78	0.85	98	135	$Cu_{12}Sb_{3.5}Sn_{0.5}S_{13}$	0.66	160.0	3.80	0.98	98	135
$Cu_{12}Sb_{3.7}Sn_{0.3}S_{13}$	0.40	200.0	1.05	0.71	99	116	$Cu_{12}Sb_3SnS_{13}$	0.30	135.0	3.23	1.25	98	135
Te doping (Sb)													
$Cu_{12}Sb_{3.9}Te_{0.1}S_{13}$	0.70	133.0	7.30	1.20	98	141	$Cu_{12}Sb_{3.2}Te_{0.8}S_{13}$	0.79	175.0	2.00	0.50	95	133
$Cu_{12}Sb_{3.9}Te_{0.1}S_{13}$	0.60	175.0	2.65	0.85	100	142	$Cu_{12}Sb_{3.6}Te_{1.4}S_{13}$	0.54	167.0	1.34	0.54	95	133
$Cu_{11.9}Ga_{0.1}Sb_{3.85}Te_{0.15}S_{14}$	0.52	149.0	5.10	1.38	98	143	$Cu_{12}Sb_{2.19}Te_{1.81}S_{13}$	0.39	250.0	0.46	0.48	95	133
$Cu_{12}Sb_{3.8}Te_{0.2}S_{13}$	0.55	180.0	2.05	0.75	99	142	$Cu_{12}Sb_{2.21}Te_{1.79}S_{13}$	0.30	220.0	0.53	0.54	95	133
$Cu_{12}Sb_{3.7}Te_{0.3}S_{13}$	0.55	185.0	1.95	0.75	99	142	$Cu_{12}Sb_{3.59}Te_{1.41}S_{13}$	0.64	212.0	1.35	0.58	93	133
$Cu_{11.8}Ga_{0.2}Sb_{3.7}Te_{0.3}S_{13}$	0.80	175.0	4.20	0.96	98	143	$Cu_{12}Sb_{2.99}Te_{1.01}S_{13}$	0.63	163.0	2.86	0.80	93	133

Open Research Europe 2026, 6:221 Last updated: 20 OCT 2026

Table 1. *Continued*

Composition	*zT*	*S* μV/K	σ S/m	κ W/(mK)	*D* %	Ref.	Composition	*zT*	*S* μV/K	σ S/m	κ W/(mK)	*D* %	Ref.
$Cu_{12}Sb_{3.6}Te_{0.4}S_{13}$	0.54	195.0	1.65	0.74	99	142	$Cu_{12}Sb_{3.48}Te_{0.52}S_{13}$	0.61	127.0	6.20	1.28	93	133
$Cu_{11.47}Co_{0.82}Sb_{3.78}Te_{0.41}S_{13}$	0.69	175.0	6.10	0.81	92	150	$Cu_{12}Sb_{2.15}Te_{1.85}S_{13}$	0.39	252.0	0.47	0.49	93	133
$Cu_{11.7}Ga_{0.3}Sb_{3.55}Te_{0.45}S_{15}$	0.67	190.0	2.80	0.85	98	143	$Cu_{12}Sb_3TeS_{12.8}Se_{0.25}$	0.74	182.0	2.63	0.72	92	148
$Cu_{12}Sb_{3.5}Te_{0.5}S_{13}$	0.70	145.0	5.10	0.99	98	141	$Cu_{12}Sb_4TeS_{12.5}Se_{0.5}$	0.53	165.0	2.74	0.80	91	148
$Cu_{12}Sb_{3.39}Te_{0.61}S_{13}$	0.76	183.0	1.82	0.50	95	133	$Cu_{12}Sb_3TeS_{12}Se$	0.51	162.0	2.75	0.83	92	148
$Cu_{12}Sb_3TeS_{13}$	0.76	180.0	2.70	0.75	98	141	$Cu_{12}Sb_3TeS_{11.5}Se_{1.5}$	0.52	163.0	3.09	0.85	95	148
Bi doping (Sb)													
$Cu_{12}Sb_{3.9}Bi_{0.1}S_{13}$	0.70	182.0	2.80	0.82	97	120	$Cu_{12}Sb_{3.7}Bi_{0.3}S_{13}$	0.50	150.0	3.50	0.95	98	120
$Cu_{11.9}Zn_{0.1}Sb_{3.9}Bi_{0.1}S_{13}$	0.55	177.0	2.50	0.87	99	112	$Cu_{11.8}Zn_{0.2}Sb_{3.6}Bi_{0.4}S_{13}$	0.42	190.0	1.20	0.67	99	112
$Cu_{12}Sb_{3.8}Bi_{0.2}S_{13}$	0.56	160.0	3.30	0.95	98	120	$Cu_{12}Sb_{3.6}Bi_{0.4}S_{13}$	0.45	160.0	2.00	0.76	99	120
$Cu_{12}Sb_{3.8}Bi_{0.2}S_{13}$	0.78	138.0	6.65	1.12	90	140	$Cu_{12}Sb_{3.6}Bi_{0.4}S_{13}$	0.71	166.0	3.90	0.96	90	140
$Cu_{11.9}Zn_{0.1}Sb_{3.8}Bi_{0.2}S_{13}$	0.51	160.0	2.90	0.97	99	112	$Cu_{12}Sb_{3.4}Bi_{0.6}S_{13}$	0.51	180.0	2.21	0.92	90	140
$Cu_{11.8}Zn_{0.2}Sb_{3.8}Bi_{0.2}S_{13}$	0.50	225.0	0.90	0.58	99	112	$Cu_{12}Sb_{3.2}Bi_{0.8}S_{13}$	0.47	178.0	1.86	0.84	90	140
S deficiency													
$Cu_{12}Sb_4S_{12.6}$	0.45	122.0	5.35	1.14	86	145	$Cu_{12}Sb_4S_{12.7}$	0.45	118.0	5.35	1.06	86	145
Se doping (S)													
$Cu_{12}Sb_4S_{12.9}Se_{0.1}$	0.50	110.0	9.40	1.48	97	146	$Cu_{12}Sb_4S_{12.6}Se_{0.4}$	0.43	212.0	1.00	0.65	96	147
$Cu_{12}Sb_4S_{12.9}Se_{0.1}$	0.58	156.0	3.70	0.95	97	147	$Cu_{11.95}Gd_{0.05}Sb_4S_{12.6}Se_{0.4}$	0.64	128.0	8.10	1.30	98	48
$Cu_{12}Sb_4S_{12.8}Se_{0.2}$	0.59	114.0	10.80	1.51	98	146	$Cu_{12}Sb_4S_{12.5}Se_{0.5}$	0.49	121.0	1.62	1.44	-	144
$Cu_{12}Sb_4S_{12.8}Se_{0.2}$	0.58	170.0	3.05	0.85	99	147	$Cu_{12}Sb_4TeS_{12.5}Se_{0.5}$	0.53	165.0	2.74	0.80	91	148
$Cu_{11.975}In_{0.025}Sb_4S_{12.8}Se_{0.2}$	0.69	120.0	8.80	1.15	95	118	$Cu_{12.5}Sb_4S_{12}Se$	0.76	124.0	7.13	0.89	95	129
$Cu_{11.95}In_{0.05}Sb_4S_{12.8}Se_{0.2}$	0.72	122.0	8.40	1.11	96	118	$Cu_{12}Sb_4S_{12}Se$	0.56	116.0	1.62	1.43	-	144
$Cu_{11.925}In_{0.075}Sb_4S_{12.8}Se_{0.2}$	0.61	126.0	7.50	1.22	96	118	$Cu_{13}Sb_4S_{12}Se$	0.78	142.4	5.59	0.91	95	129
$Cu_{12}Sb_3TeS_{12.8}Se_{0.25}$	0.74	182.0	2.63	0.72	92	148	$Cu_{12}Sb_3TeS_{12}Se$	0.51	162.0	2.75	0.83	92	148
$Cu_{12}Sb_4S_{12.7}Se_{0.3}$	0.52	115.0	9.40	1.48	98	146	$Cu_{12}Sb_3TeS_{11.5}Se_{1.5}$	0.52	163.0	3.09	0.85	95	148
$Cu_{12}Sb_4S_{12.7}Se_{0.3}$	0.50	173.0	1.70	0.60	97	147	$Cu_{12}Sb_4S_{11}Se_2$	0.47	120.0	1.62	1.43	-	144
$Cu_{12}Sb_4S_{12.6}Se_{0.4}$	0.48	123.0	8.60	1.61	97	146							

Open Research Europe 2026, 6:221 Last updated: 20 OCT 2026

Acknowledgment

During manuscript preparation, ChatGPT version 5.5 was used solely to improve clarity and flow; it was not involved in analysis, interpretation, or scientific decision-making. The authors reviewed and approved all content and assume full responsibility for the final manuscript.

References

1. Forman C, Muritala IK, Pardemann R, *et al.*: **Estimating the global waste heat potential.** *Renew. Sust. Energ. Rev.* 2016; **57**: 1568–1579.
Publisher Full Text

2. Gayner C, Kar KK: **Recent advances in thermoelectric materials.** *Prog. Mater. Sci.* 2016; **83**: 330–382.
Publisher Full Text

3. Baskaran P, Rajasekar M: **Recent trends and future perspectives of thermoelectric materials and their applications.** *RSC Adv.* 2024; **14**: 21706–21744.
PubMed Abstract | Publisher Full Text | Free Full Text

4. Caballero-Calero O, Ares JR, Martín-González M: **Environmentally friendly thermoelectric materials: High performance from inorganic components with low toxicity and abundance in the earth.** *Adv. Sustainable Syst.* 2021; **5**.
Publisher Full Text

5. Pourkiaei SM, Ahmadi MH, Sadeghzadeh M, *et al.*: **Thermoelectric cooler and thermoelectric generator devices: A review of present and potential applications, modeling and materials.** *Energy.* 2019; **186**: 115849.
Publisher Full Text

6. Mamur H, Dilmaç ÖF, Begum J, *et al.*: **Thermoelectric generators act as renewable energy sources.** *Cleaner Mater.* 2021; **2**: 100030.
Publisher Full Text

7. Chen J, Zuo L, Wu Y, *et al.*: **Modeling, experiments and optimization of an on-pipe thermoelectric generator.** *Energy Convers. Manag.* 2016; **122**: 298–309.
Publisher Full Text

8. Ambrosi RM, Williams H, Watkinson EJ, *et al.*: **European radioisotope thermoelectric generators (RTGs) and radioisotope heater units (RHUs) for space science and exploration.** *Space Sci. Rev.* 2019; **215**: 55.
Publisher Full Text

9. Konstantinou G, Kyratsi T, Louca LS: **Design of a thermoelectric device for power generation through waste heat recovery from marine internal combustion engines.** *Energies.* 2022; **15**: 4075.

10. Gao H, Huang G, Li H, *et al.*: **Development of stove-powered thermoelectric generators: A review.** *Appl. Therm. Eng.* 2016; **96**: 297–310.
Publisher Full Text

11. Penumala SM, Karmel A, Kanimozhi G, *et al.*: **Thermoelectric generator powered timepiece circuit for rechargeable battery operation.** *Sci. Rep.* 2024; **14**: 1–17.
Publisher Full Text

12. He X, Shi XL, Wu X, *et al.*: **Three-dimensional flexible thermoelectric fabrics for smart wearables.** *Nat. Commun.* 2025; **16**: 2523.
PubMed Abstract | Publisher Full Text | Free Full Text

13. Sootsman J, Chung D, Kanatzidis M: **New and old concepts in thermoelectric materials.** *Angew. Chem. Int. Ed.* 2009; **48**: 8616–8639.
PubMed Abstract | Publisher Full Text

14. He J, Tritt TM: **Advances in thermoelectric materials research: Looking back and moving forward.** *Science.* 2017; **357**.
PubMed Abstract | Publisher Full Text

15. Majumdar A: **Thermoelectricity in semiconductor nanostructures.** *Science.* 2004; **303**: 777–778.

16. Vining CB: **An inconvenient truth about thermoelectrics.** *Nat. Mater.* 2009; **8**: 83–85.
PubMed Abstract | Publisher Full Text

17. Zhao D, Tan G: **A review of thermoelectric cooling: Materials, modeling and applications.** *Appl. Therm. Eng.* 2014; **66**: 15–24.
Publisher Full Text

18. Patyk A: **Thermoelectrics: Impacts on the environment and sustainability.** *J. Electron. Mater.* 2010; **39**: 2023–2028.
Publisher Full Text

19. Kishita Y, Ohishi Y, Uwasu M, *et al.*: **Evaluating the life cycle CO_2 emissions and costs of thermoelectric generators for passenger automobiles: a scenario analysis.** *J. Clean. Prod.* 2016; **126**: 607–619.
Publisher Full Text

20. Feng M, Lv S, Deng J, *et al.*: **An overview of environmental energy harvesting by thermoelectric generators.** *Renew. Sust. Energ. Rev.* 2023; **187**: 113723.
Publisher Full Text

21. Skinner BJ, Luce FD, Makovicky E: **Studies of the sulfosalts of copper III; Phases and phase relations in the system Cu-Sb-S.** *Econ. Geol.* 1972; **67**: 924–938.
Publisher Full Text

22. Johnson NE, Craig JR, Rimstidt JD: **Crystal chemistry of tetrahedrite.** *Am. Mineral.* 1988; **73**: 389–397.

23. Lu X, Morelli DT: **Natural mineral tetrahedrite as a direct source of thermoelectric materials.** *Phys. Chem. Chem. Phys.* 2013; **15**: 5762–5766.
PubMed Abstract | Publisher Full Text

24. Lu X, Morelli DT, Xia Y, *et al.*: **High performance thermoelectricity in earth-abundant compounds based on natural mineral tetrahedrites.** *Adv. Energy Mater.* 2013; **3**: 342–348.
Publisher Full Text

25. Neves F, Esperto L, Figueira I, *et al.*: **Mechanochemical synthesis of tetrahedrite materials using mixtures of synthetic and ore samples collected in the Portuguese zone of the Iberian Pyrite Belt.** *Miner. Eng.* 2021; **164**: 106833.
Publisher Full Text

26. Barroso A, Henriques R, Cerqueira A, *et al.*: **Acid mine drainage and waste dispersion in legacy mining sites: An integrated approach using UAV photogrammetry and geospatial analysis.** *J. Hazard. Mater.* 2025; **495**: 138827.
PubMed Abstract | Publisher Full Text

27. Dehkordi AM, Zebarjadi M, He J, *et al.*: **Thermoelectric power factor: Enhancement mechanisms and strategies for higher performance thermoelectric materials.** *Mater. Sci. Eng. R. Rep.* 2015; **97**: 1–22.
Publisher Full Text

28. Snyder GJ, Snyder AH: **Figure of merit ZT of a thermoelectric device defined from materials properties.** *Energy Environ. Sci.* 2017; **10**: 2280–2283.
Publisher Full Text

29. Beretta D, Neophytou N, Hodges JM, *et al.*: **Thermoelectrics: From history, a window to the future.** *Mater. Sci. Eng. R. Rep.* 2019; **138**: 100501.
Publisher Full Text

30. Goldsmid HJ, Douglas RW: **The use of semiconductors in thermoelectric refrigeration.** *Br. J. Appl. Phys.* 1954; **5**: 386–390.
Publisher Full Text

31. Nair SS, Singh N: **Mechanisms and design principles for optimizing lattice thermal conductivity in chalcogenides: A comprehensive review.** *Mater. Today Phys.* 2025; **57**: 101785.
Publisher Full Text

32. Snyder GJ, Toberer ES: **Complex thermoelectric materials.** *Nat. Mater.* 2008; **7**: 105–114.
Publisher Full Text

33. Suekuni K, Tsuruta K, Ariga T, *et al.*: **Thermoelectric properties of mineral tetrahedrites $Cu_{10}Tr_2Sb_4S_{13}$ with low thermal conductivity.** *Appl. Phys. Express.* 2012; **5**: 051201.
Publisher Full Text

34. Makovicky E, Forcher K, Lottermoser W, *et al.*: **The Role of Fe^{2+} and Fe^{3+} in synthetic Fe-substituted tetrahedrite.** *Mineral. Petrol.* 1990; **43**: 73–81.
Publisher Full Text

35. Wuensch BJ: **The crystal structure of tetrahedrite, $Cu_{12}Sb_4S_{13}$.** *Z. Krist.* 1964; **119**: 437–453.
Publisher Full Text

36. Pfitzner A, Evain M, Petricek V: **$Cu_{12}Sb_4S_{13}$: A temperature-dependent structure investigation.** *Acta Crystallographica Section B Structural Science.* 1997; **53**: 337–345.
Publisher Full Text

37. Long SO, Powell AV, Hull S, *et al.*: **Jahn–Teller driven electronic instability in thermoelectric tetrahedrite.** *Adv. Funct. Mater.* 2020; **30**.
Publisher Full Text

38. Dolyniuk J-A, Owens-Baird B, Wang J, *et al.*: **Clathrate thermoelectrics.** *Mater. Sci. Eng. R. Rep.* 2016; **108**: 1–46.
Publisher Full Text

39. Lai W, Wang Y, Morelli DT, *et al.*: **From bonding asymmetry to anharmonic rattling in $Cu_{12}Sb_4S_{13}$ tetrahedrites: When lone-pair electrons are not so lonely.** *Adv. Funct. Mater.* 2015; **25**: 3648–3657.
Publisher Full Text

40. Maji K, Raveau B, Lemoine P, *et al.*: **Open PDF Three-fold coordination of copper in sulfides: A blockade for hole carrier delocalization but a driving force for ultralow thermal conductivity.** *J. Am. Chem. Soc.* 2024; **146**: 9741–9754.
PubMed Abstract | Publisher Full Text

41. Suekuni K, Lee CH, Tanaka HI, *et al.*: **Retreat from stress: Rattling in a planar coordination.** *Adv. Mater.* 2018; **30**: e1706230.
PubMed Abstract | Publisher Full Text

42. Momma K, Izumi F: **VESTA 3 for three-dimensional visualization of crystal, volumetric and morphology data.** *J. Appl. Crystallogr.* 2011; **44**: 1272–1276.
Publisher Full Text

43. Tippireddy S, Chetty R, Naik MH, *et al.*: **Electronic and thermoelectric properties of transition metal substituted tetrahedrites.** *J. Phys. Chem. C.* 2018; **122**: 8735–8749.
Publisher Full Text

44. Raveau B: **Copper mixed valence concept:"Cu(I)-Cu (II)" in thermoelectric copper sulfides-an alternative to "Cu (II)-Cu (III)" in superconducting cuprates.** *J. Supercond. Nov. Magn.* 2020; **33**: 259–263.
Publisher Full Text

45. Biagioni C, George LL, Cook NJ, *et al.*: **The tetrahedrite group: Nomenclature and classification.** *Am. Mineral.* 2020; **105**: 109–122.
Publisher Full Text

46. Pattrick RAD, van der Laan G, Vaughan DJ, *et al.*: **Oxidation state and electronic configuration determination of copper in tetrahedrite group minerals by L-edge X-ray absorption spectroscopy.** *Phys. Chem. Miner.* 1993; **20**: 395–401.
Publisher Full Text

47. Chetty R, Bali A, Naik MH, *et al.*: **Thermoelectric properties of Co-substituted synthetic tetrahedrite.** *Acta Mater.* 2015; **100**: 266–274.
Publisher Full Text

48. Rout U, Mallik RC: **Thermoelectric properties of Gd and Se double substituted tetrahedrite.** *Dalton Trans.* 2024; **53**: 3511–3522.
PubMed Abstract | Publisher Full Text

49. Buckley AN, Skinner WM, Harmer SL, *et al.*: **Examination of the proposition that Cu (II) can be required for charge neutrality in a sulfide lattice — Cu in tetrahedrites and sphalerite.** *Can. J. Chem.* 2007; **85**: 767–781.
Publisher Full Text

50. Suekuni K, Tomizawa Y, Ozaki T, *et al.*: **Systematic study of electronic and magnetic properties for $Cu_{12-x}TM_xSb_4S_{13}$ (TM= Mn, Fe, Co, Ni, and Zn) tetrahedrite.** *J. Appl. Phys.* 2014; **115**.
Publisher Full Text

51. Baláž P: **Review of reserved deposits of metals in slovakia.** *Slovak Geological Magazine.* 2015; **15**: 31–38.

52. Gaspar OC: **Mineralogy and sulfide mineral chemistry of the Neves Corvo ores, Portugal: Insight into their Genesis.** *Can. Mineral.* 2002; **40**: 611–636.
Publisher Full Text

53. Dong Z, Jiang T, Xu B, *et al.*: **Density functional theory study on electronic structure of tetrahedrite and effect of natural impurities on its flotation property.** *Miner. Eng.* 2021; **169**: 106980.
Publisher Full Text

54. Katsura Y, Kumagai M, Mato T, *et al.*: **Starrydata: from published plots to shared materials data.** *Science and Technology of Advanced Materials: Methods.* 2025; **5**.
Publisher Full Text

55. Candolfi C, Bouyrie Y, Sassi S, *et al.*: *Tetrahedrites: Prospective novel thermoelectric materials.* InTech; 2016.

56. Chetty R, Bali A, Mallik RC: **Tetrahedrites as thermoelectric materials: An overview.** *J. Mater. Chem. C.* 2015; **3**: 12364–12378.
Publisher Full Text

57. Weller DP, Morelli DT: **Tetrahedrite thermoelectrics: From fundamental science to facile synthesis.** *Frontiers in Electronic Materials.* 2022; **2**.
Publisher Full Text

58. Polak MP, Morgan D: **Leveraging Vision Capabilities of Multimodal LLMs for Automated Data Extraction from Plots.** 2025.

59. Rohatgi A: **WebPlotDigitizer (Version 5).** 2015.
Reference Source

60. Quitério C, Rajput K, Marchand D, *et al.*: **Tetrahedrites for thermoelectric applications: A database.** *ZENODO.* 2025.

61. Coelho R, Moço D, de Sá AI, *et al.*: **Tetrahedrite nanocomposites for high performance thermoelectrics.** *Nanomaterials.* 2025; **15**: 351.
PubMed Abstract | Publisher Full Text | Free Full Text

62. Hu H, Sun F-H, Dong J, *et al.*: **Nanostructure engineering and performance enhancement in Fe2 O3 -dispersed $Cu_{12}Sb_4S_{13}$ thermoelectric composites with earth-abundant elements.** *ACS Appl. Mater. Interfaces.* 2020; **12**: 17852–17860.
PubMed Abstract | Publisher Full Text

63. Sun F-H, Dong J, Tang H, *et al.*: **Enhanced performance of thermoelectric nanocomposites based on $Cu_{12}Sb_4S_{13}$ tetrahedrite.** *Nano Energy.* 2019; **57**: 835–841.
Publisher Full Text

64. Shi X, Wu A, Liu W, *et al.*: **Polycrystalline SnSe with extraordinary thermoelectric property via nanoporous design.** *ACS Nano.* 2018; **12**: 11417–11425.
PubMed Abstract | Publisher Full Text

65. Fasana CD, Jensen MS, García Ponte GE, *et al.*: **Synthetic versatility, reaction pathway, and thermal stability of tetrahedrite nanoparticles.** *J. Mater. Chem. C.* 2020; **8**: 14219–14229.
Publisher Full Text

66. Nakada T, Takahashi M, Shijimaya C, *et al.*: **Gram-Scale synthesis of tetrahedrite nanoparticles and their thermoelectric properties.** *Langmuir.* 2019; **35**: 16335–16340.
PubMed Abstract | Publisher Full Text

67. Sun F-H, Dong J, Tang H, *et al.*: **ZnO-nanoparticle dispersed $Cu_{11.5}Ni_{0.5}Sb_4S_{13-\delta}$ tetrahedrite composites with enhanced thermoelectric performance.** *J. Electron. Mater.* 2019; **48**: 1840–1845.
Publisher Full Text

68. Dobrozhan O, Pshenychnyi R, Klymov O, *et al.*: **Synthesis and characterization of nanostructured tetrahedrite and its composite with dielectric inclusions.** *Mater. Sci. Semicond. Process.* 2024; **182**: 108690.
Publisher Full Text

69. Wei Y, Liu J, Cheng Z, *et al.*: **Synthesis-temperature-dependent phase composition manipulation toward high thermoelectric performance in tetrahedrites.** *J. Mater. Sci. Technol.* 2024; **168**: 124–130.
Publisher Full Text

70. Santos BA, Esperto L, Figueira I, *et al.*: **Thermoelectric properties of tetrahedrites produced from mixtures of natural and synthetic materials.** *Materials.* 2025; **18**: 1375.
PubMed Abstract | Publisher Full Text | Free Full Text

71. Levinsky P, Vaney J-B, Candolfi C, *et al.*: **Electrical, thermal, and magnetic characterization of natural tetrahedrites–tennantites of different origin.** *J. Electron. Mater.* 2016; **45**: 1351–1357.
Publisher Full Text

72. James DJ, Lu X, Morelli DT, *et al.*: **Solvothermal synthesis of tetrahedrite: Speeding up the process of thermoelectric material generation.** *ACS Appl. Mater. Interfaces.* 2015; **7**: 23623–23632.
PubMed Abstract | Publisher Full Text

73. Zazakowny K, Kosonowski A, Lis A, *et al.*: **Phase analysis and thermoelectric properties of Cu-rich tetrahedrite prepared by solvothermal synthesis.** *Materials.* 2022; **15**: 849.
PubMed Abstract | Publisher Full Text | Free Full Text

74. Weller DP, Morelli DT: **Rapid synthesis of zinc and nickel co-doped tetrahedrite thermoelectrics by reactive spark plasma sintering and mechanical alloying.** *J. Alloys Compd.* 2017; **710**: 794–799.
Publisher Full Text

75. Lis A, Zazakowny K, Cherniushok O, *et al.*: **Nanostructured $Cu_{12+x}Sb_{4-x}S_{13}$ tetrahedrites prepared by solvothermal synthesis in 1-(2-aminoethyl) piperazine for efficient thermal energy**

harvesting. *J. Alloys Compd.* 2024; **977**: 173337.
Publisher Full Text

76. Baláž P, Briančin J, Turčániová L: **Thermal decomposition of mechanically activated tetrahedrite.** *Thermochim. Acta.* 1995; **249**: 375–381.
Publisher Full Text

77. López Cota FA, Díaz-Guillén JA, Juan Dura O, *et al.*: **Mechanosynthesis and thermoelectric properties of Fe, Zn, and Cd-doped P-type tetrahedrite: $Cu_{12-x}M_xSb_4S_{13}$.** *Materials.* 2021; **14**: 3448.
PubMed Abstract | Publisher Full Text | Free Full Text

78. Kresse G, Furthmuller J: **Efficient iterative schemes for ab initio total energy calculations using a plane-wave basis set.** *Physical reviews B: Condensed matter and materials physics.* 1996; **54**: 11169–11186.
Publisher Full Text

79. Kresse G, Furthmuller J: **Efficiency of ab-initio total energy calculations for metals and semiconductors using a plane-wave basis set.** *Comput. Mater. Sci.* 1996; **6**: 15–50.
Publisher Full Text

80. Blochl PE: **Projector augmented-wave method.** *Physical reviews B: Condensed matter and materials physics.* 1994; **50**: 17953–17979.
Publisher Full Text

81. Perdew JP, Burke K, Ernzerhof M: **Generalized gradient approximation made simple.** *Phys. Rev. Lett.* 1996; **77**: 3865–3868.
Publisher Full Text

82. Sun J, Ruzsinszky A, Perdew JP: **Strongly constrained and appropriately normed semilocal density functional.** *Phys. Rev. Lett.* 2015; **115**: 036402.
Publisher Full Text

83. Quitério C, Rajput K, Iordanidou K, *et al.*: **Supplementary Information for Hidden processing drivers of thermoelectric performance in tetrahedrites.** *ZENODO.* 2026.
Publisher Full Text

84. Rogl G, Rogl PF: **Filled Sb-based skutterudites from 1996–2022.** *Crystals.* 2022; **12**: 1843.
Publisher Full Text

85. Gaultois MW, Sparks TD, Borg CKH, *et al.*: **Data-driven review of thermoelectric materials: Performance and resource considerations.** *Chem. Mater.* 2013; **25**: 2911–2920.
Publisher Full Text

86. Wang H, Bai S, Chen L, *et al.*: **International round-robin study of the thermoelectric transport properties of an n-type half-Heusler compound from 300 K to 773 K.** *J. Electron. Mater.* 2015; **44**: 4482–4491.
Publisher Full Text

87. Wei T-R, Guan M, Yu J, *et al.*: **How to measure thermoelectric properties reliably.** *Joule.* 2018; **2**: 2183–2188.
Publisher Full Text

88. Alleno E, Bérardan D, Candolfi C, *et al.*: **A round-robin test of the uncertainty on the measurement of the thermoelectric dimensionless figure of merit of $Co_{0.97}Ni_{0.03}Sb_3$.** *Rev. Sci. Instrum.* 2015; **86**: 011301.
PubMed Abstract | Publisher Full Text

89. Baláž P, Achimovičová M, Baláž M, *et al.*: **Hallmarks of mechanochemistry: from nanoparticles to technology.** *Chem. Soc. Rev.* 2013; **42**: 7571–7637.
PubMed Abstract | Publisher Full Text

90. Suryanarayana C: **Mechanical alloying: A novel technique to synthesize advanced materials.** *Research.* 2019; **2019**: 4219812.
Publisher Full Text

91. Yvon P, Schwarz R: **Effects of iron impurities in mechanical alloying using steel media.** *J. Mater. Res.* 1993; **8**: 239–241.
Publisher Full Text

92. Moravčík I, Kubíček A, de Almeida M, *et al.*: **The origins of high-Entropy alloy contamination induced by mechanical alloying and sintering.** *Metals.* 2020; **10**: 1186.

93. Kang S-JL: *Sintering: Densification, Grain Growth and Microstructure.* Elsevier Butterworth-Heinemann;1st ed 2005.

94. Vaqueiro P: *Inorganic Thermoelectric Materials: From Fundamental Concepts to Materials Design.* Powell AV, editor. The Royal Society of Chemistry; 2021; pp. 1–52. ch. 1.

95. Hulbert DM, Anders A, Dudina DV, *et al.*: **The absence of plasma in "spark plasma sintering.".** *J. Appl. Phys.* 2008; **104**.
Publisher Full Text

96. Suekuni K, Tsuruta K, Kunii M, *et al.*: **High-performance thermoelectric mineral $Cu_{12-x}Ni_xSb_4S_{13}$ tetrahedrite.** *J. Appl. Phys.* 2013; **113**.

97. Battiston S, Fanciulli C, Fiameni S, *et al.*: **One step synthesis and sintering of Ni and Zn substituted tetrahedrite as thermoelectric material.** *J. Alloys Compd.* 2017; **702**: 75–83.
Publisher Full Text

98. LeBlanc S: **Thermoelectric generators: Linking material properties and systems engineering for waste heat recovery applications.** *Sustain. Mater. Technol.* 2014; **1-2**: 26–35.
Publisher Full Text

99. Sarma DD: **Essential considerations for reporting thermoelectric properties.** *ACS Energy Lett.* 2021; **6**: 3715–3718.

100. Heo J, Laurita G, Muir S, *et al.*: **Enhanced thermoelectric performance of synthetic tetrahedrites.** *Chem. Mater.* 2014; **26**: 2047–2051.
Publisher Full Text

101. Coelho R, Symeou E, Kyratsi T, *et al.*: **Tetrahedrite sintering conditions: The $Cu_{11}Mn_1Sb_4S_{13}$ case.** *J. Electron. Mater.* 2020; **49**: 5077–5083.
Publisher Full Text

102. Barbier T, Lemoine P, Gascoin S, *et al.*: **Structural stability of the synthetic thermoelectric ternary and nickel-substituted tetrahedrite phases.** *J. Alloys Compd.* 2015; **634**: 253–262.
Publisher Full Text

103. Prem Kumar DS, Chetty R, Rogl P, *et al.*: **Thermoelectric properties of Cd doped tetrahedrite: $Cu_{12-x}Cd_xSb_4S_{13}$.** *Intermetallics.* 2016; **78**: 21–29.
Publisher Full Text

104. Gonçalves AP, Lopes EB, Montemor MF, *et al.*: **Oxidation studies of $Cu_{12}Sb_{3.9}Bi_{0.1}S_{10}Se_3$ tetrahedrite.** *J. Electron. Mater.* 2018; **47**: 2880–2889.
Publisher Full Text

105. Sun F-H, Dong J, Dey S, *et al.*: **Enhanced thermoelectric performance of $Cu_{12}Sb_4S_{13}$ – tetrahedrite via nickel doping.** *Sci. China-Mater.* 2018; **61**: 1209–1217.
Publisher Full Text

106. Pi J-H, Lee GE, Kim IH: **Effects of aging on thermoelectric properties of tetrahedrite $Cu_{12}Sb_4S_{13}$.** *J. Korean Phys. Soc.* 2019; **74**: 865–870.

107. Pi J-H, Lee G-E, Kim IH: **Thermal stability, mechanical properties and thermoelectric performance of $Cu_{11}TrSb_4S_{13}$ (Tr=Mn, Fe, Co, Ni, Cu, and Zn).** *J. Electron. Mater.* 2020; **49**: 2710–2718.
Publisher Full Text

108. Prem Kumar DS, Tippireddy S, Ramakrishnan A, *et al.*: **Thermoelectric and electronic properties of chromium substituted tetrahedrite.** *Semicond. Sci. Technol.* 2019; **34**: 035017.
Publisher Full Text

109. Baláž P, Guilmeau E, Daneu N, *et al.*: **Tetrahedrites synthesized via scalable mechanochemical process and spark plasma sintering.** *J. Eur. Ceram. Soc.* 2020; **40**: 1922–1930.
Publisher Full Text

110. Kim S-Y, Pi J-H, Lee G-E, *et al.*: **Synthesis of Fe-doped tetrahedrites $Cu_{12-x}Fe_xSb_4S_{13}$ and characterization of their thermoelectric properties.** *Korean Journal of Metals and Materials.* 2020; **58**: 340–347.
Publisher Full Text

111. Kim S-Y, Lee G-E, Kim I-H: **Synthesis and thermoelectric Properties of $Cu_{12-x}Ni_xSb_4S_{13}$ tetrahedrites.** *J. Electron. Mater.* 2020; **49**: 2775–2780.
Publisher Full Text

112. Lee G-E, Kim I-H: **Effects of Zn/Bi double doping on the charge transport and thermoelectric properties of tetrahedrites $Cu_{12-x}Zn_xSb_{4-y}Bi_yS_{13}$.** *J. Electron. Mater.* 2020; **49**: 2768–2774.
Publisher Full Text

113. Huang L, Kong Y, Zhang J, *et al.*: **Effects of Sb deviation from its stoichiometric ratio on the micro- and electronic structures and thermoelectric properties of $Cu_{12}Sb_4S_{13}$.** *ACS Appl. Mater. Interfaces.* 2020; **12**: 14145–14153.
PubMed Abstract | Publisher Full Text

114. Hu H, Zhuang HL, Jiang Y, *et al.*: **Thermoelectric $Cu_{12}Sb_4S_{13}$-based synthetic minerals with a sublimation-derived porous network.** *Adv. Mater.* 2021; **33**: e2103633.
PubMed Abstract | Publisher Full Text

115. Tippireddy S, Ghosh S, Biswas R, *et al.*: **Thermoelectric properties of Al substituted tetrahedrite.** *J. Appl. Phys.* 2020; **127**.
Publisher Full Text

116. Ahn H-J, Kim I-H: **Charge transport and thermoelectric properties of Sn-doped tetrahedrites $Cu_{12}Sb_{4-y}Sn_yS_{13}$.** *Korean Journal of Metals and Materials.* 2021; **59**: 724–731.
Publisher Full Text

117. Jeong S-I, Kim I-H: **Solid-State synthesis and thermoelectric properties of Ge-doped tetrahedrites $Cu_{12}Sb_{4-y}Ge_yS_{13}$.** *Korean Journal of Metals and Materials.* 2022; **60**: 376–383.
Publisher Full Text

118. Zhu C, Ming H, Zhang J, *et al.*: **Ultralow lattice thermal Conductivity and high thermoelectric figure of merit in dually**

substituted $Cu_{12}Sb_4S_{13}$ tetrahedrites. *Advanced Electronic Materials.* 2022; **8**: 2200110.
Publisher Full Text

119. Ojha A, Anirudh R, Bathula S: **Augmentation in the thermoelectric performance by integrating the natural minerals with synthetic tetrahedrite compounds.** *Mater. Sci. Semicond. Process.* 2024; **180**: 108562.
Publisher Full Text

120. Kwak S-G, Pi J-H, Lee G-E, *et al.*: **Solid-state synthesis and thermoelectric properties of tetrahedrites $Cu_{12}Sb_{4-y}Bi_yS_{13}$.** *Korean Journal of Metals and Materials.* 2020; **58**: 272–277.
Publisher Full Text

121. Torquato S: *Random Heterogeneous Materials: Microstructure and Macroscopic Properties.* Springer; 2002.

122. Chen G, Dresselhaus MS, Dresselhaus G, *et al.*: **Recent developments in thermoelectric materials.** *Int. Mater. Rev.* 2003; **48**: 45–66.
Publisher Full Text

123. Xia Y, Ozoliņš V, Wolverton C: **Microscopic mechanisms of glasslike lattice thermal transport in cubic $Cu_{12}Sb_4S_{13}$ tetrahedrites.** *Phys. Rev. Lett.* 2020; **125**: 085901.
PubMed Abstract | Publisher Full Text

124. May AF, Delaire O, Niedziela JL, *et al.*: **Structural phase transition and phonon instability in $Cu_{12}Sb_4S_{13}$.** *Phys. Rev. B.* 2016; **93**: 064104.
Publisher Full Text

125. Nakagawa J, Kage Y, Hori T, *et al.*: **Crystal structure dependent thermal conductivity in two-dimensional phononic crystal nanostructures.** *Appl. Phys. Lett.* 2015; **107**.
Publisher Full Text

126. Andreasen JW, Makovicky E, Lebech B, *et al.*: **The role of iron in tetrahedrite and tennantite determined by Rietveld refinement of neutron powder diffraction data.** *Phys. Chem. Miner.* 2008; **35**: 447–454.
Publisher Full Text

127. Vaqueiro P, Guélou G, Kaltzoglou A, *et al.*: **The Influence of mobile copper ions on the glass-like thermal conductivity of copper-rich tetrahedrites.** *Chem. Mater.* 2017; **29**: 4080–4090.
Publisher Full Text

128. Kwak S-G, Kim I-H: **Thermoelectric properties of the off-stoichiometric tetrahedrites $Cu_{12+m}Sb_4S_{13}$.** *J. Korean Phys. Soc.* 2022; **80**: 1054–1059.
Publisher Full Text

129. Yan Y, Wu H, Wang G, *et al.*: **High thermoelectric performance balanced by electrical and thermal transport in tetrahedrites $Cu_{12+x}Sb_4S_{12}Se$.** *Energy Storage Mater.* 2018; **13**: 127–133.
Publisher Full Text

130. Lu X, Morelli DT, Xia Y, *et al.*: **Increasing the thermoelectric figure of merit of tetrahedrites by co-doping with nickel and zinc.** *Chem. Mater.* 2015; **27**: 408–413.
Publisher Full Text

131. Moço D, Malta JF, Santos LF, *et al.*: **Thermoelectric properties of nickel and selenium co-doped tetrahedrite.** *Materials.* 2023; **16**: 898.
PubMed Abstract | Publisher Full Text | Free Full Text

132. Weller D, Kunkel G, Ochs A, *et al.*: **Observation of n-type behavior in Fe-doped tetrahedrite at low temperature.** *Mater. Today Phys.* 2018; **7**: 1–6.
Publisher Full Text

133. Bouyrie Y, Candolfi C, Ohorodniichuk V, *et al.*: **Crystal structure, electronic band structure and high-temperature thermoelectric properties of Te-substituted tetrahedrites $Cu_{12}Sb_{4-x}Te_xS_{13}$ ($0.5 \leq x \leq 2.0$).** *J. Mater. Chem. C.* 2015; **3**: 10476–10487.
Publisher Full Text

134. Chetty R, Prem Kumar DS, Rogl G, *et al.*: **Thermoelectric properties of a Mn substituted synthetic tetrahedrite.** *Phys. Chem. Chem. Phys.* 2015; **17**: 1716–1727.
PubMed Abstract | Publisher Full Text

135. Tippireddy S, Prem Kumar DS, Karati A, *et al.*: **Effect of Sn substitution on the thermoelectric properties of synthetic tetrahedrite.** *ACS Appl. Mater. Interfaces.* 2019; **11**: 21686–21696.
PubMed Abstract | Publisher Full Text

136. Zhu C, Chen Q, Ming H, *et al.*: **Improved thermoelectric performance of $Cu_{12}Sb_4S_{13}$ through Gd substitution induced enhancement of electronic density of states and phonon scattering.** *ACS Appl. Mater. Interfaces.* 2021; **13**: 25092–25101.
PubMed Abstract | Publisher Full Text

137. Charnock JM, Garner CD, Pattrick RAD, *et al.*: **EXAFS and MÖssbauer spectroscopic study of Fe bearing tetrahedrites.** *Mineral. Mag.* 1989; **53**: 193–199.
Publisher Full Text

138. Nasonova DI, Presniakov IA, Sobolev AV, *et al.*: **Role of iron in synthetic tetrahedrites revisited.** *J. Solid State Chem.* 2016; **235**: 28–35.
Publisher Full Text

139. Sobolev AV, Presniakov IA, Nasonova DI, *et al.*: **Thermally activated electron exchange in $Cu_{12-x}Te_xSb_{4-x}S_{13}$ ($x = 1.3, 1.5$) tetrahedrites: A MÖssbauer study.** *J. Phys. Chem. C.* 2017; **121**: 4548–4557.
Publisher Full Text

140. Prem Kumar DS, Chetty R, Femi OE, *et al.*: **Thermoelectric properties of Bi-doped tetrahedrite.** *J. Electron. Mater.* 2017; **46**: 2616–2622.
Publisher Full Text

141. Lu X, Morelli D: **The effect of Te substitution for Sb on thermoelectric properties of tetrahedrite.** *J. Electron. Mater.* 2014; **43**: 1983–1987.
Publisher Full Text

142. Kwak S-G, Lee G-E, Kim I-H: **Electronic transport and thermoelectric properties of Te-doped tetrahedrites $Cu_{12}Sb_{4-y}Te_yS_{13}$.** *Korean Journal of Metals and Materials.* 2021; **59**: 560–566.

143. Yang C, Qu L, Wang P, *et al.*: **Improved thermoelectric performance in Ga- and Te-Cointroduced tetrahedrite $Cu_{12}Sb_4S_{13}$.** *Adv. Eng. Mater.* 2024; **26**.
Publisher Full Text

144. Lu X, Morelli DT, Wang Y, *et al.*: **Phase stability, crystal structure, and thermoelectric properties of $Cu_{12}Sb_4S_{13-x}Se$ solid solutions.** *Chem. Mater.* 2016; **28**: 1781–1786.
Publisher Full Text

145. Sun FH, Wu CF, Li Z, *et al.*: **Powder metallurgically synthesized $Cu_{12}Sb_4S_{13}$ tetrahedrites: phase transition and high thermoelectricity.** *RSC Adv.* 2017; **7**: 18909–18916.

146. Zhu C, Ming H, Huang L, *et al.*: **Achieving high power factor and thermoelectric performance through dual substitution of Zn and Se in tetrahedrites $Cu_{12}Sb_4S_{13}$.** *Appl. Phys. Lett.* 2019; **115**.
Publisher Full Text

147. Kwak S-G, Lee G-E, Kim I-H: **Effects of Se doping on thermoelectric properties of tetrahedrite $Cu_{12}Sb_4S_{13-z}Se_z$.** *Electron. Mater. Lett.* 2021; **17**: 164–171.
Publisher Full Text

148. Bouyrie Y: **Identification, synthèse et caractérisation de phases tétraédrites pour la conversion d'énergie par effets thermoélectriques.** 2015. Ph.D. thesis.

149. Ellmer K: **Hall effect and conductivity measurements in semiconductor crystals and thin Films.** *Characterization of Materials.* Kaufmann EN, editor. Wiley; 2012; 1–16.

150. Bouyrie Y, Sassi S, Candolfi C, *et al.*: **Thermoelectric properties of double-substituted tetrahedrites $Cu_{12-x}Co_xSb_{4-y}Te_yS_{13}$.** *Dalton Trans.* 2016; **45**: 7294–7302.
PubMed Abstract | Publisher Full Text

151. Yan Y, Li N, Wang G, *et al.*: **Achieving high average power factor in tetrahedrite $Cu_{12}Sb_4S_{13}$ via regulating electron-phonon coupling strength.** *Mater. Today Phys.* 2022; **22**: 100590.

152. Lupu NZ, Tallan NM, Tannhauser DS: **Apparatus for measuring the Hall effect of low-mobility samples at high temperatures.** *Rev. Sci. Instrum.* 1967; **38**: 1658–1661.
Publisher Full Text

153. Kwak S-G, Lee G-E, Kim I-H: **Electronic transport and thermoelectric properties of $Cu_{12-x}Zn_xSb_4S_{13}$ tetrahedrites prepared by mechanical alloying and hot pressing.** *Korean Journal of Metals and Materials.* 2019; **57**: 328–333.
Publisher Full Text

154. Morelli DT, Lu X: **Thermoelectric materials based on tetrahedrite structure for thermoelectric devices.** *US 10,622,534, United States Patent and Trademark Office.* Apr. 2020.

155. Kosaka Y, Suekuni K, Hashikuni K, *et al.*: **Effects of Ge and Sn substitution on the metal–semiconductor transition and thermoelectric properties of $Cu_{12}Sb_4S_{13}$ tetrahedrite.** *Phys. Chem. Chem. Phys.* 2017; **19**: 8874–8879.

156. Weller DP, Morelli DT: **Rapid synthesis of zinc and nickel co-doped tetrahedrite thermoelectrics by reactive spark plasma sintering and mechanical alloying.** *J. Alloys Compd.* 2017; **710**: 794–799.
Publisher Full Text

157. Chen K: *Synthesis and thermoelectric properties of Cu-Sb-S compounds.* Queen Mary, University of London; 2016. Ph.D. thesis.

158. Kim S-Y, Kwak S-G, Pi J-H, *et al.*: **Preparation of tetrahedrite $Cu_{12}Sb_4S_{13}$ by mechanical alloying and hot pressing.** *J. Electron.*

Mater. 2019; **48**: 1857–1863.
Publisher Full Text

159. Huang LL, Wang YS, Zhu C, *et al.*: **Preparation and enhanced thermoelectric performance of Pb-doped tetrahedrite $Cu_{12-x}Pb_xSb_4S_{13}$.** *J. Alloys Compd.* 2018; **769**: 478–483.
Publisher Full Text

160. Levinský P, Ventrapati PK, Dauscher A, *et al.*: **Achieving high thermoelectric performance in mixed natural-synthetic tetrahedrites.** *ChemNanoMat.* 2022; **8**.
Publisher Full Text

161. Wang JY, Li XY, Bao YF: **Thermoelectric properties of Mn dopped $Cu_{12-x}Mn_xSb_4S_{13}$ tetrahedrites.** *Mater. Sci. Forum.* 2016; **847**: 161–165.
Publisher Full Text

162. Levinsky P, Candolfi C, Dauscher A, *et al.*: **Thermoelectric properties of magnesium-doped tetrahedrite $Cu_{12-x}Mg_xSb_4S_{13}$.** *J. Electron. Mater.* 2019; **48**: 1926–1931.
Publisher Full Text

163. Kim S-Y, Lee G-E, Kim I-H: **Thermoelectric properties of mechanically alloyed and hot-pressed $Cu_{12-x}Co_xSb_4S_{13}$ tetrahedrites.** *J. Korean Phys. Soc.* 2019; **74**: 967–971.
Publisher Full Text

164. Harish S, Sivaprahasam D, Battabyal M, *et al.*: **Phase stability and thermoelectric properties of $Cu_{10.5}Zn_{1.5}Sb_4S_{13}$ tetrahedrite.** *J. Alloys Compd.* 2016; **667**: 323–328.
Publisher Full Text